

On obtaining neutron-star mass and radius constraints from quiescent low-mass X-ray binaries in the Galactic plane

Alessio Marino¹*, N. Degenaar², T. Di Salvo¹, R. Wijnands², L. Burderi³ and R. Iaria¹

¹Università degli Studi di Palermo, Dipartimento di Fisica e Chimica, via Archirafi 36 - 90123 Palermo, Italy

²Anton Pannekoek Institute for Astronomy, University of Amsterdam, Postbus 94249, 1090 GE Amsterdam The Netherlands

³Università degli Studi di Cagliari, Dipartimento di Fisica, SP Monserrato-Sestu km 0.7, I-09042 Monserrato, Italy

Accepted XXX. Received YYY; in original form ZZZ

ABSTRACT

X-ray spectral analysis of quiescent low-mass X-ray binaries (LMXBs) has been one of the most common tools to measure the radius of neutron stars (NSs) for over a decade. So far, this method has been mainly applied to NSs in globular clusters, primarily because of their well-constrained distances. Here, we study *Chandra* data of seven transient LMXBs in the Galactic plane in quiescence to investigate the potential of constraining the radius (and mass) of the NSs inhabiting these systems. We find that only two of these objects had X-ray spectra of sufficient quality to obtain reasonable constraints on the radius, with the most stringent being an upper limit of $R \lesssim 14.5$ km for EXO 0748–676 (for assumed ranges for mass and distance). Using these seven sources, we also investigate systematic biases on the mass/radius determination; for Aql X-1 we find that omitting a power-law spectral component when it does not seem to be required by the data, results in peculiar trends in the obtained radius with changing mass and distance. For EXO 0748–676 we find that a slight variation in the lower limit of the energy range chosen for the fit leads to systematically different masses and radii. Finally, we simulated *Athena* spectra and found that some of the biases can be lifted when higher quality spectra are available and that, in general, the search for constraints on the equation of state of ultra-dense matter via NS radius and mass measurements may receive a considerable boost in the future.

Key words: accretion, accretion discs – dense matter – equation of state – stars: neutron – X-rays: binaries

1 INTRODUCTION

Matter in the interiors of neutron stars (NSs) is found in extreme conditions (for instance a density at least ~ 2 – 5 times higher than the nuclear density), and hence requires a special equation of state (EoS) of ultra-dense matter to describe the composition and behaviour. The dense-matter EoS determines the mass (M) and radius (R) of a NS by means of the Tolman-Oppenheimer-Volkoff equations and results in specific $M - R$ curves for each EoS (see Özel & Freire 2016, for a recent review). Each EoS is characterized by a maximum mass, resulting from the fact that all EoSs have a maximum central density beyond which no stable configuration is possible.

Dozens of possible $M - R$ relations have been developed in the past few decades (see e.g. Lattimer 2012), all allowed within our current understanding of NSs. The credibility of different EoSs to describe NS interiors cannot be tested with terrestrial experiments, because it is impossible to reach the required extreme densities and, at same time, the low temperatures relevant for NSs in

any laboratory on Earth. This is therefore an astrophysical task: directly measuring masses and radii of NSs, or even only obtaining some constraints on these parameters, can tell us if a theoretical EoS is plausible or not.

Unfortunately it is not easy to measure both the radius and the mass of a single NS. Whereas masses have been reliably determined for a number of radio pulsars through radio pulsar timing techniques (e.g. Özel & Freire 2016), it is very challenging to determine the radii of these NSs (see Watts et al. 2015, for a recent discussion and outlook). Without a measurement of both M and R for the same NS, it is only the most extreme mass measurements, near and above $\sim 2 M_{\odot}$, that start to put some interesting constraints on the dense-matter EoS (e.g. Demorest et al. 2010; Antoniadis et al. 2013; Hebeler et al. 2013; Fonseca et al. 2016; Fortin et al. 2017).

In the past decade, some relevant steps forward have been made in estimating the radii of NSs through the development of various techniques. Nearly all of these rely on X-ray spectroscopy and the most promising ones involve analyzing the thermal emission emerging from the surface of the hot NSs in low mass X-ray binaries (LMXBs). This surface emission provides the means to directly measure their apparent angular size and extract information

* E-mail: alessio.marino@unipa.it

on the radius. However, to convert the radius observed in infinity to the true NS radius requires to take into account gravitational effects, so that the NS mass enters the equations as well; in practice a combined mass/radius pair is thus measured. If independent constraints can be obtained, for instance on the gravitational redshift or on the dynamical mass, the degeneracy can be broken and both M and R can be obtained (e.g. Özel 2006).

The surface emission from NSs is often overwhelmed by other emission processes in LMXBs, most prominently the X-rays from the accretion flow, but it is visible under a number of circumstances. For instance, M and R measurements can in principle be obtained from observations of thermonuclear X-ray bursts (simply X-ray bursts hereafter), because the NS surface then briefly outshines the accretion flow (e.g. Ebisuzaki 1987; van Paradijs & Lewin 1990; Lewin et al. 1993; Zamfir et al. 2012; Özel & Freire 2016; Nättilä et al. 2016). Furthermore, some NSs channel the accretion flow along their magnetic field lines creating visible surface hotspots; the resulting X-ray pulse profiles can be a powerful tool to extract information on the NS mass and radius (e.g. Pavlov & Zavlin 1997; Nath et al. 2002; Poutanen & Gierliński 2003; Leahy et al. 2008; Lo et al. 2013; Miller & Lamb 2015; Bogdanov et al. 2016).

A third method, which is the focus of the present work, consists of analyzing the quiescent thermal emission from transient LMXBs; the heat radiation released from these systems during the phase in which the accretion has (nearly) switched off. In this quiescent state these sources are ~ 4 – 5 orders of magnitude fainter than during their active accretion episodes, with an X-ray luminosity of $\approx 10^{32}$ – 10^{33} erg s $^{-1}$. The heat radiated from the surface is thought to be generated in nuclear reactions (e.g. Haensel & Zdunik 2003) that occur in the crust during accretion phases (Brown & Bildsten (1998); see Wijnands et al. (2017) for an observational review).

The spectrum emerging from a NS is expected to be a blackbody reprocessed and modulated by the interactions with the stellar atmosphere. When a NS is in quiescence this thin layer is expected to be made of mostly H (or He if the companion is a degenerate star), because heavier elements should settle on short time scales. To obtain reliable mass/radius measurements from studying the thermal surface emission of NS LMXBs, it is vital to model the atmosphere correctly (e.g. Zavlin et al. 1996; Rutledge et al. 1999; Suleimanov et al. 2011; Servillat et al. 2012; Nättilä et al. 2015). Several theoretical models have been developed to describe the quiescent thermal emission of the weakly magnetized ($B \lesssim 10^9$ G) NSs in LMXBs, assuming different compositions of the atmosphere (e.g. Zavlin et al. 1996; Heinke et al. 2006; Ho & Heinke 2009; Haakonsen et al. 2012).

Sometimes the emission from a quiescent LMXB (qLMXB hereafter) cannot be properly described by a simple NS atmosphere model due to the presence, often quite evident from the spectrum, of a hard emission tail that dominates over the thermal component at energies $\gtrsim 3$ keV (e.g. Asai et al. 1998; Rutledge et al. 1999; Jonker et al. 2004; Cackett et al. 2011; Fridriksson et al. 2011a; Chakrabarty et al. 2014; Parikh et al. 2017a).¹ The physical origin of this emission, usually modeled as a simple power law, is not clear but several possible explanations have been suggested in the past; these include residual accretion on to the NS surface and different

emission processes related to the magnetic field of the NS (e.g. Campana et al. 1998; Degenaar et al. 2012b; Chakrabarty et al. 2014; D’Angelo et al. 2015; Wijnands et al. 2015).

Inferring NS radii from their quiescent thermal emission is promising, but subject to various systematic uncertainties. First of all, since the thermal emission essentially provides a measurement of the angular size, uncertainties in the source distance translate directly into uncertainties in the inferred radii. Moreover, apart from the effect of technical issues such as pile-up (e.g. Bogdanov et al. 2016), the (often unknown) atmosphere composition has a large impact on radius measurements of NS LMXBs (e.g. Servillat et al. 2012; Catuneanu et al. 2013; Heinke et al. 2014). Biases are also introduced if the surface temperature of the NS is inhomogeneous (Elshamouty et al. 2016); this could occur for instance if residual accretion takes place, which we know to happen in at least some sources (e.g. Cackett et al. 2010a; Fridriksson et al. 2011a; D’Angelo et al. 2015). Local channeling of heat from the interior along magnetic field lines can also potentially generate hotspots on the NS surface that bias the measurements (Elsner & Lamb 1977; Ikhsanov 2001; Lii et al. 2014; Rouco Escorial et al. 2017). Finally, many NSs also spin very rapidly, which causes them to be oblate and their surface radiation to be Doppler boosted. However, these effects are smaller than the typical systematic uncertainties involved in EOS determinations and are therefore typically uncorrected for in this method (e.g. Steiner et al. 2013).

1.1 Motivation for the present work

So far, mostly globular clusters have been exploited to measure NS radii and masses from the quiescent thermal emission. Among their often low interstellar extinction and their relative abundance in these environments, a primary advantage of using NSs in globular clusters is their typically well-constrained distances opposed to field LMXBs (e.g. Heinke et al. 2003a, 2014; Webb & Barret 2007; Guillot et al. 2013; Bogdanov et al. 2016; Steiner et al. 2018). Furthermore, qLMXBs in globular clusters often have purely thermal spectra, i.e. that do not require a hard emission component to be modeled, and show no temporal variations (with some exceptions; e.g. Heinke et al. 2003b; Degenaar & Wijnands 2012; Bahramian et al. 2015). The absence of a power-law component in the X-ray spectra and lack of variability suggests that there is no ongoing accretion that could hamper obtaining reliable constraints on the NS parameters.

Nevertheless, there are also some drawbacks of using qLMXBs in globular clusters for this approach. In particular, most of the sources used in this kind of analysis have never exhibited an outburst and have faint companion stars, so that the composition of the NS atmosphere is not known. This is a concern because many LMXBs in globular clusters may have H-poor donor stars (e.g. Bahramian et al. 2014); as mentioned above, uncertainties in the composition of the atmosphere have a huge effect on the determination of NS radii.

Field LMXBs have the complication that their distances are often not accurately known (current uncertainties are at the level of 10% or higher; e.g. Jonker & Nelemans 2004), their quiescent spectra often contain a power-law spectral component (e.g. Jonker et al. 2004), and their quiescent emission can vary irregularly on time scales of hours to years (e.g. Rutledge et al. 2002a; Campana & Stella 2003). The latter two features are often taken as evidence that some residual accretion is ongoing (e.g. Cackett et al. 2010a; Wijnands et al. 2015). However, field LMXBs also offer certain advantages for NS mass and radius determinations. For instance,

¹ The hard power-law tail in the quiescent spectra of NS LMXBs is often referred to as “non-thermal” because it deviates from the soft thermal spectral component that is ascribed to the NS surface emission. However, Bremsstrahlung emission from a boundary layer is a viable mechanism for the harder spectral component, so indicating it as non-thermal is strictly not correct; see D’Angelo et al. (2015).

field LMXBs have typically undergone one or more accretion outbursts during which the companion type and/or composition of the accreted matter could be determined. Furthermore, during those outbursts the X-ray emission may be pulsed or X-ray bursts may be observed, which can provide independent measurements of M and R . What further adds to field LMXBs as promising tests for the dense-matter EOS is that additional, indirect constraints on NS radii may come from measurements of the accretion flow properties (obtained during outbursts), such as the localization of the inner accretion disk via X-ray reflection spectroscopy (e.g. Bhattacharyya 2010; Miller et al. 2013; Chiang et al. 2016; Ludlam et al. 2017; Matranga et al. 2017), or studies of kHz and mHz quasi-periodic oscillations (QPOs; e.g. Miller et al. 1998; van Straaten et al. 2000; Barret et al. 2006; Stiele et al. 2016). Although these measurements are typically not constraining by itself, there is some potential in combining them with more direct measurements for improved constraints on M and R , and to cross-calibrate different methods (e.g. Watts et al. 2016, for a discussion). Another argument in favour of field LMXBs is that sometimes the companion stars are bright enough to allow for optical dynamical mass measurements during their quiescent states (e.g. Orosz & Kuulkers 1999; Elebert et al. 2009; Casares et al. 2010; Wang et al. 2013; Mata Sánchez et al. 2017); although current constraints are not strong, these can possibly be improved with large upcoming facilities. Finally, it is important to explore how useful quiescent field LMXBs are for precise NS mass and radius measurements because new sensitive X-ray instruments, like the scheduled mission *Athena* (see Section 5), will not have the sub-arcsecond spatial resolution that is typically needed to resolve the globular cluster sources.

In this work we present a dedicated X-ray spectral analysis of seven LMXBs, located in the Galactic plane, during their quiescent states. This study is aimed, on one hand, to constrain masses and radii of the NSs inhabiting these systems, and on the other hand to investigate the main biases and weak spots of applying this method to field LMXBs.

2 SAMPLE AND DATA SELECTION

For our study, we searched the literature for NS LMXBs in the field (i.e. globular cluster sources were not considered) that have been observed in quiescence with sensitive X-ray instruments (see Section 3). In total, quiescent data are available for ~ 49 NS LMXBs (see Wijnands et al. 2017, for a recent overview). Detailed studies of the thermal emission of NS LMXBs requires high sensitivity at soft X-ray energies ($\lesssim 3$ keV), and are therefore best carried out with the *Chandra* or *XMM-Newton* observatories. To refrain from possibly introducing an additional bias in our analysis related to instrument cross-calibration (e.g. Degenaar et al. 2011), we here choose to focus solely on *Chandra* data. A source suitable for our study needs to fulfill the following additional requirements: i) the quiescent spectrum has a thermal emission component, ii) the *Chandra* quiescent spectrum is of sufficient quality to test if there is a hard emission tail, iii) the source has a reasonably accurate distance estimate (e.g. from X-ray bursts).

Requirement i) listed above rules out some well-studied sources that have power-law dominated quiescent spectra, such as SAX J1808–3654 (e.g. Campana et al. 2002; Heinke et al. 2007, 2009), or NSs located near the Galactic center for which virtually all soft thermal emission is absorbed due to the very high interstellar extinction ($N_{\text{H}} \gtrsim 5 \times 10^{22} \text{ cm}^{-2}$; e.g. Degenaar et al. 2012a). In practice, requirement ii) often implies that a source needs to

be relatively bright or have multiple observations taken in quiescence. This rules out quite a number of NS LMXBs that were observed only once in quiescence by the *Chandra* observatory, have low signal-to-noise spectra, or are not detected (e.g. Tomsick et al. 2004; Cornelisse et al. 2007; Jonker et al. 2007a,b; Degenaar et al. 2017). Finally, requirement iii) unfortunately rules out a source like MAXI J0556–332, which is bright and well-studied in quiescence, but for which the available distance estimates are not model independent and rely on some assumptions about the M and R of the NS in the system (Homan et al. 2014; Parikh et al. 2017b).

Based on the above three criteria, we initially selected seven NS LMXBs for our analysis. Four of these, KS 1731–260, XTE J1701–462, MXB 1659–29 and EXO 0748–676, have been observed multiple times in quiescence to study the thermal evolution of the NS crust after an outburst (see Wijnands et al. 2017, for a review and Appendix A for source-specific references). In addition to these crust-cooling sources, the relatively nearby NS LMXBs Cen X-4 and Aql X-1 have been observed in quiescence many times (e.g. Cackett et al. 2010a, 2011; Campana et al. 2014, for compilations) and are thus good targets for our study. Lastly, we included 4U 1608–52 in our analysis. Although this NS has been observed in quiescence only once, its quiescent spectrum is of decent quality and some constraints on its mass and radius have previously been obtained from the analysis of its X-ray bursts (Poutanen et al. 2014) and disk reflection (Degenaar et al. 2015). It therefore seemed a promising target for our study. The seven sources in our sample are briefly described in Appendix A. The main properties that are relevant for the present work are summarized in Table 1.

3 DATA REDUCTION AND ANALYSIS

Table 2 gives an overview of the observations included in our study. We note that KS 1731–260, XTE J1701–462 and MXB 1659–29 have more *Chandra* observations in quiescence than we used here. This is because for KS 1731–260 and XTE J1701–462 we soon found that the small number of photons collected at energies $\lesssim 3$ keV (due to a low flux and/or relatively high absorption column density) did not allow us to obtain meaningful constraints on the NS mass and radius (see Section 4.1). In case of MXB 1659–29, the spectra taken at later times had significantly lower quality due to cooling of the NS crust (and hence fading of the thermal X-ray emission; Cackett et al. 2006, 2013b). Therefore we decided not to include more spectra for those three sources. For EXO 0748–676, Cen X-4, Aql X-1 and 4U 1608–52, we did use all available *Chandra* data.

All observations listed in Table 2 were obtained with the ACIS-S, sometimes using a sub-array to avoid pile-up. Exposure times varied between 4.7–42.9 ks for individual spectra. We refer the reader to the references in Table 2 for details on the different observations. We here only quote the full details of the single *Chandra* observation of 4U 1608–52, as to our knowledge those data have not been published previously. *Chandra* observed 4U 1608–52 on 2010 October 11 starting at 03:15 UT for a duration of 23 ks. The observation was performed with the ACIS-S in a 1/8 sub-array and using the faint, timed data mode. There were no background flares during the observation, so all data could be used in the analysis.

Data processing, reduction and spectral extraction of all observations was performed within CIAO v. 4.9. The raw data were first put through a number of reprocessing steps consisting of applying the latest available calibration, removing episodes of background flaring and applying good time intervals. After those steps, the re-

Source name	ν_{spin} (Hz)	P_{orb} (hr)	D (kpc)	Reference D	$N_{\text{H}}^{\text{Gal}}$ (10^{21} cm^{-2})	Previous R (and M) constraints	Reference R (and M)
KS 1731–260	524	-	$\lesssim 8$	[1,2]	3.1	$R < 12 \text{ km}, M < 1.8 M_{\odot}$	[2]
XTE J1701–462	-	-	8.8 ± 1.3	[3]	7.2	-	-
MXB 1659–29	567	7.1	7–15	[4,5]	1.8	-	-
EXO 0748–676	552	3.8	7.1 ± 1.2	[5]	1.0	$M = 2.00^{+0.07}_{-0.24} M_{\odot}$ and $R = 11.3^{+1.3}_{-1.0} \text{ km}$ (0.3–10 keV)	[6]
						$M = 1.50^{+0.4}_{-1.0} M_{\odot}$ and $R = 12.2^{+0.8}_{-3.6} \text{ km}$ (0.5–10 keV)	[6]
Cen X-4	-	15.1	1.2 ± 0.3	[7]	0.9	$R = 7 - 12.5 \text{ km}$ for $M = 1.5 M_{\odot}$	[8]
Aql X-1	550	19	3.5–8	[5,9,10]	2.8	see Section A6	[11]
4U 1608–52	620	$\sim 12?$	2.9 – 7.8	[5]	18	$R > 12 \text{ km}$ for $M = 1.0 - 2.4 M_{\odot}$ $R < 21 \text{ km}$ for $M = 1.5 M_{\odot}$	[12] [13]

Table 1. Summary of the main properties of the NS LMXBs in our sample relevant for the present study. For reference, we quote the Galactic absorption in the direction of each source, $N_{\text{H}}^{\text{Gal}}$, which reflects the weighted average value of Kalberla et al. (2005). References: 1=Muno et al. (2000a), 2=Özel et al. (2012), 3=Lin et al. (2009), 4=Oosterbroek et al. (2001), 5=Galloway et al. (2008a), 6=Cheng et al. (2017), 7=Chevalier et al. (1989), 8=Cackett et al. (2010a), 9=Rutledge et al. (2001b), 10=Mata Sánchez et al. (2017), 11=Li et al. (2017), 12=Poutanen et al. (2014), 13=Degenaar et al. (2015).

Target	ObsID	Date (mm-dd-yyyy)	Reference	Net counts
KS 1731–260	2428	03-27-2001	[1–7]	174±13
XTE J1701–462	7513	08-12-2017	[8,9]	200±14
MXB 1659-298	2688	10-15-2001	[10–13]	30.35±5
	3794	10-16-2002		259(16)
EXO 0748–676	9070	10-12-2008	[14–16]	3190±50
	10783	10-15-2008		3150±60
	9072	06-10-2009		4280±60
	10871	02-25-2009		1710±40
	11059	04-20-2010		3920±40
	12414	07-02-2011		5430±70
	11060	10-20-2013		3760±60
	14663	08-01-2013		3900±60
Cen X-4	713	06-23-2000	[17,18]	2670±50
	4576	06-21-2004		960±30
Aql X-1	708	11-28-2000	[19–24]	1230±30
	709	02-19-2001		740±30
	710	03-23-2001		860±30
	711	04-20-2001		1140±30
	3484	05-05-2002		1060±30
	3485	05-20-2002		1280±40
	3486	06-11-2002		2250±50
	3487	07-05-2002		580±20
	3488	07-22-2002		590±20
	3489	08-18-2002		580±20
	3490	09-03-2002		720±30
	12457	10-22-2010		1620±40
	12458	10-30-2010		920±30
	12459	11-12-2010		1000±30
4U 1608-52	12470	10-11-2010	this work	930±30

Table 2. List of all *Chandra* ACIS-S observations used in this work. References: 1=Wijnands et al. (2001b), 2=Wijnands et al. (2002), 3=Rutledge et al. (2002b), 4=Cackett et al. (2006), 5=Cackett et al. (2010b), 6=Zurita et al. (2010), 7=Merritt et al. (2016), 8=Fridriksson et al. (2010), 9=Fridriksson et al. (2011b), 10=Wijnands et al. (2003), 11=Wijnands et al. (2004), 12=Cackett et al. (2008), 13=Cackett et al. (2013b), 14=Degenaar et al. (2009), 15=Degenaar et al. (2011), 16=Degenaar et al. (2014), 17=Cackett et al. (2010a), 18=Rutledge et al. (2001a), 19=Rutledge et al. (2001b), 20=Rutledge et al. (2002a), 21=Campana & Stella (2003), 22=Li et al. (2017), 23=Cackett et al. (2011), 24=Campana et al. (2014).

processed data were suitable for spectral extraction. Source spectra were obtained using a $\sim 1''$ -radius circular region, with the exact size depending on the source brightness. A background spectrum was extracted from the same image using a circular region with a radius three times larger than that of the source and placed well away from it. The routine SPEXTRACT was used to create the spectra and build the ancillary response files (arfs) and the redistribution matrix files (rmfs). All spectra were rebinned using the tool

GRPPHA into channels with a minimum of 20 counts per bin, so that χ^2 statistics could be used to probe the goodness of the spectral fits.

Since MXB 1659–29 displays X-ray eclipses we reduced the exposure time of the spectra by 900 s per eclipse, to make sure that we obtain the correct X-ray flux (and spectral parameters) during our fits. Similarly, the spectra of EXO 0748–676 were corrected; in this source the eclipses last for 500 s. To determine the times of eclipses during our observations we used the ephemeris of Ooster-

broek et al. (2001) for MXB 1659–29 and of Wolff et al. (2009) for EXO 0748–676.²

We estimated the level of pile-up in each of the analyzed observations, using the web version of PIMMS (Portable Interactive Multi-Mission Simulator), which uses the proportionality between the pile-up fraction and the true count-rate to estimate the level of pile-up in a data set. For none of the data considered in this work the pile-up fraction exceeded 6%, which we deemed sufficiently small to leave uncorrected in the scope of the present work. Although it was demonstrated that even a pile-up level of 1% can affect the M and R constraints (Bogdanov et al. 2016), we are not after precision measurements in this work and the effect of pile-up will be much smaller than other biases such as e.g. the distance uncertainty.

All spectral fits were performed within XSPEC (v. 12.9.1), ignoring all data outside the energy range of 0.3–10 keV. Five of the sources in our sample (MXB 1659–29, EXO 0748–676, Cen X-4, Aql X-1 and 4U 1608–52) have orbital information that rule out an ultra-compact nature (see Appendix A). For the remaining two sources (KS 1731–260 and XTE J1701–462) there are no direct constraints on their orbital parameters, although their X-ray burst or accretion properties suggest that these both accrete H-rich material too (Galloway et al. 2008a; Lin et al. 2009). Moreover the luminous outbursts experienced by both sources seem to disfavor very small orbits and hence H-deficient donor stars (Shahbaz et al. 1998; Meyer-Hofmeister 2004; Wu et al. 2010).³ A H-atmosphere should thus be appropriate to model the thermal spectra of the NSs in our sample. We choose to use NSATMOS (Heinke et al. 2006), which has five fit parameters: the NS effective temperature (T_{eff}), mass (M), and radius (R), which are all in the NS frame, as well as the source distance (D) and a normalization factor. The latter parametrizes the fraction of the surface that is emitting the thermal radiation; this parameter was fixed to 1 in all fits (i.e. we assume a homogeneously emitting NS). In addition to the thermal emission component, we tested for and modeled any possible hard emission tail using PEGPWRLW. This model is characterized by a power-law index Γ and a normalization that gives the unabsorbed flux of the power-law component in the energy range that is specified by the remaining two parameters (for which we took 0.5–10 keV). Finally, we modeled the interstellar absorption (N_{H}) using the TBABS model (Wilms et al. 2000) with VERN cross-sections (Verner et al. 1996) and ANGR abundances (Anders & Grevesse 1989).

To reduce the number of free parameters during the spectral fits, the distance to the source was always fixed (but we did probe a distance range) to a value compatible with that reported in literature (see Table 1). This strategy leaves N_{H} , T_{eff} , M and R as free parameters, together with Γ and the power-law normalization in case a hard emission tail was modeled. When multiple spectra were available for a single source, those spectra were fitted simultaneously with the parameters that are not expected to change over time (e.g. the N_{H} , the distance, NS mass and radius) tied between the different data sets. To reduce the number of degeneracies, we also decided

to tie the Γ indices relative to the various spectra. However, the NS temperature and power-law normalization were always allowed to freely vary between different data sets, as those are known to change over time for all our sources.

For each source, our first step was to choose the right model to describe the spectrum and to evaluate the need for including a power-law component in the spectral fits. To this aim, we fitted each of the observations with both a single thermal model, TBABS×NSATMOS, and one with an additional hard power-law tail, TBABS×(NSATMOS+PEGPWRLW). We then employed the standard practice to test the significance of the non-thermal component via an f-test (FTEST in XSPEC), which estimates the probability that the improvement in χ^2 due to the addition of an extra component, in our case a power-law, to the model is occurring by chance. If the obtained f-test probability was on the order of 10^{-3} or larger, we considered the contribution of the non-thermal component not significant. The power-law component was kept in the model when the f-test results gave a much smaller probability.

Without very good statistics, the attempt of constraining the NS mass and radius at the same time usually resulted in huge error bars on all spectral parameters. We therefore applied an alternative approach in which we focused on obtaining the radius of the NS and probed how the best-fit radius changed when stepping the mass through a range of reasonable values. In other words, in this strategy several fits were launched for the same spectrum leaving, in each of them, M fixed to a different value in the range of 1–2 M_{\odot} . This range is motivated based on the approximate range between the lowest measured NS mass (one of the NSs in the double-NS system J0453+1559, with a mass of $1.174 \pm 0.004 M_{\odot}$; Martinez et al. 2015) and the highest one (the current record-holder J0348+0432 with a mass of $2.01 \pm 0.04 M_{\odot}$; Antoniadis et al. 2013).

All the best-fit radii individuated by the fits form a wide range which, under the hypothesis that the model correctly describes these spectra, includes the real radius of the NS. The associated errors to the estimated values were initially calculated using the ERROR command, which individuates, for a specified parameter, the 90% confidence region of it, exploring the χ^2 landscape around the best-fit radius. We then improved the precision of these results applying a Goodman-Weare algorithm of Monte Carlo Markov Chain (MCMC; Goodman & Weare 2010), appropriate in the case of a skewed and elongated distribution for mass and radius, using the command CHAIN in XSPEC. Whenever the mass value was frozen, the MCMC procedure was launched with 300 walkers and a chain length of 9000, whereas when both M and R were left free in the fit, we used 200 chains, each of length equal to 2×10^6 . The errors reported in this work, unless otherwise specified, were calculated with the ERROR command for the resulting simulated posterior distribution and reflect 90% confidence intervals.

4 CHANDRA RESULTS

Out of the seven sources in our sample, we were able to obtain meaningful constraints on R (and M) for only two NS LMXBs, EXO 0748–676 and Aql X-1, which we describe in Section 4.2. For the other five sources it was not possible to constrain the NS parameters. In Section 4.1 we argue that the main limitation is the number of counts in the spectra. Nevertheless, the search for exact NS masses and radii was not the main aim of this work; rather we wanted to test how constraining and reliable the results for field LMXBs may be in general, and in particular to probe the effect of some of the biases mentioned in Section 1. The data quality for

² In case of MXB 1659–29, the only *Chandra* observation used in this work contained a single eclipse, so the exposure time was reduced with 900 s accordingly. In case of EXO 0748–676 we reduced the exposure time with 500 s for observations 9070, 10783, 10871, with 1000 s for observations 9072, 11059, 11060 and with 1500 s for observations 12414 and 14663, depending on whether one, two or three eclipses occurred.

³ In any case, we could not obtain constraints on M and R from the quiescent thermal emission of KS 1731–260 and XTE J1701–462. The uncertainty in their atmosphere composition is thus not a concern for the present work.

EXO 0748–676 and Aql X-1 allowed us to explicitly test the effect of the energy range over which the spectra are fitted, the presence of a power-law spectral component, and distance uncertainties. We present and discuss these results in Sections 4.3, 4.4 and 4.5, respectively.

4.1 The effect of limited statistics

The failure to obtain strong constraints on the stellar parameters for most of the NSs in our sample likely has different reasons. To this extent, we can divide our targets into different groups. The first group is composed of KS 1731–260, XTE J1701–462 and MXB 1659–29; these three NSs have been observed with *Chandra* multiple times in quiescence and hence appeared good targets for our study. However, as can be seen in Table 2, a limited number of counts ($\lesssim 300$ counts) are obtained for these three sources due to their low fluxes. In case of XTE J1701–462 the absorption column is also relatively high ($\sim 10^{22}$ cm $^{-2}$; see Table 1), which further reduces the thermal flux and hence any constraints on the NS parameters obtained from it. Furthermore, XTE J1701–462 contains a significant power-law component, which further adds to the uncertainties (see below). Nevertheless, KS 1731–260 and MXB 1659–29 have a lower column density and purely thermal spectrum, but still no constraints on M and R can be obtained. Clearly, having only a few hundreds of counts per spectrum is not sufficient to obtain any meaningful constraints on the NS parameters.

The second group of sources is then composed of Cen X-4 and 4U 1608–52. The spectra obtained for these sources are of much higher quality ($\sim 900 - 2700$ counts per spectrum) than that of the first group, yet no strong constraints on M and R can be obtained. For 4U 1608–52 we suspect that its relatively high absorption ($\sim 10^{22}$ cm $^{-2}$) plays a role, but this is certainly not the case for Cen X-4 (see Table 1). What might be an issue is that these two sources contain a significant power-law component in their spectra; this adds two free parameters in the spectral fits (the power-law index and normalization) and may also create degeneracies (e.g. a positive correlation between radius and power-law index) that limit the constraints that can be obtained on the NS parameters.

In case of Cen X-4, the power-law spectral component contributes $\sim 50\%$ to the total unabsorbed 0.5–10 keV flux (see also Cackett et al. 2010a), whereas this is $\sim 20\%$ for 4U 1608–52. Nevertheless, Aql X-1 also contains a similarly strong power-law component in some of its X-ray spectra (e.g. Cackett et al. 2011, see also Section 4.4) and yet we do obtain good constraints for that NS. Since Aql X-1 has been observed with *Chandra* in quiescence much more often (14 times) than 4U 1608–52 (only once) and Cen X-4 (only twice), this suggests that statistics is the main limiting factor. This is confirmed by our *Athena* simulations presented in Section 5, where we found that strong constraints on the NS parameters can be obtained for 4U 1608–52 with much better data, despite its relatively high column density and considerable power-law spectral component. It thus appears that particularly in case of a power-law emission tail and a high absorption column density, spectra with at least several thousands of counts are required to measure the NS parameters.

Having put up front that no constraints can be obtained for any of the NSs in these five quiescent LMXBs, we briefly give some more detail about the results obtained for the individual sources. For KS 1731–260 and MXB 1659–29, the high value of the f-test probability suggested their spectra could be described by a purely thermal model. XTE J1701–462, Cen X-4 and 4U 1608–52, on the other hand, were modeled with the inclusion of a power-law com-

ponent. For KS 1731–260, XTE J1701–462 and 4U 1608–52, the errors of R pegged at the lower and upper limits hence no probable radius range could be isolated.

For MXB 1659–29 we were able to obtain limits on the NS radius, but only with very large errors; the best-fit radii are comprised in the range 6–20 km for NS masses of 1–2 M_{\odot} . For Cen X-4, our analysis procedure led to a range of 5–17 km for the radius of its NS (for $M = 1-2 M_{\odot}$). We can compare these results to that of Cackett et al. (2010a) where the radius of the Cen X-4 was measured to be $R = 7 - 12.5$ km for $M = 1.5 M_{\odot}$ at a confidence level of 68%, via the analysis of combined *Chandra*, *XMM-Newton*, *Suzaku* and *ASCA* observations. This is compatible with our result; assuming a mass of $M = 1.5 M_{\odot}$ for Cen X-4, we obtain a radius measurement of $R = 5 - 15$ km at a confidence level of 90%. For both MXB 1659–29 and Cen X-4 the obtained radius ranges are so wide that they comprise basically all EoSs ever hypothesized, so no interesting constraints are obtained.

4.2 Constraints for EXO 0748–676 and Aql X-1

For all eight spectra of EXO 0748–676, an f-test does not yield evidence of a strong power-law component in the spectrum. We therefore fitted all data of this source using a NS atmosphere model only. Due to the high number of counts in the spectra (see Table 2), the final results for the radius are comprised in a relatively small range of 9–12 km (see Table B1), which can be seen in Figure 1 (top, purple). The full results for these fits can be found in Table B1. The quality of the data allowed us to find constraints on both the mass and the radius of the NS, yielding $M = 1.65^{+0.11}_{-0.80} M_{\odot}$ and $R = 10^{+2}_{-1}$ km for an assumed distance of 7.1 kpc (see Table 3). These results are consistent within the (large) errors with the findings of Cheng et al. (2017) using *XMM-Newton* quiescent data (see Section 4.3). For EXO 0748–676 we investigated the effect of the energy range considered for the spectral fits on the obtained NS mass and radius. These results are included in Figure 1 (top, green) and Table 3, but are discussed in detail separately in Section 4.3. In Section 4.5 we discuss the effect of the distance uncertainty on the radius constraints for EXO 0748–676.

Using an f-test as a diagnostic of the need to include a power-law spectral component, we found that for Aql X-1 the data could be split into two samples, depending on whether or not they required a power-law component (see Section 4.4). However, as we argue in Sections 4.4 and 4.5, it appears that likely all spectra of Aql X-1 include a hard emission tail. Therefore, we here report on the mass and radius results obtained for this NS by fitting all of its 14 *Chandra* spectra with a composite model of a NS atmosphere and an additional power-law component. The results of these fits are shown in Figure 1 (bottom), and yield radii between 10 and 15 km (see also Table B2). Leaving the mass to be a free fit parameter and assuming a distance of 5 kpc (see Section 4.5 for a discussion on the distance bias), we were able to constrain the mass and radius simultaneously, albeit with large errors: $M = 1.8^{+0.4}_{-0.9} M_{\odot}$ and $R = 10.2^{+3.2}_{-1.5}$ km (see Table 3).

4.3 EXO 0748–676: Dependence on the fitted energy range

In all our analysis we fitted the *Chandra* spectral data over an energy range of 0.3–10 keV. Recently, Cheng et al. (2017) used *XMM-Newton* data of EXO 0748–676 in quiescence to infer the NS parameters, and found that the results strongly depended on

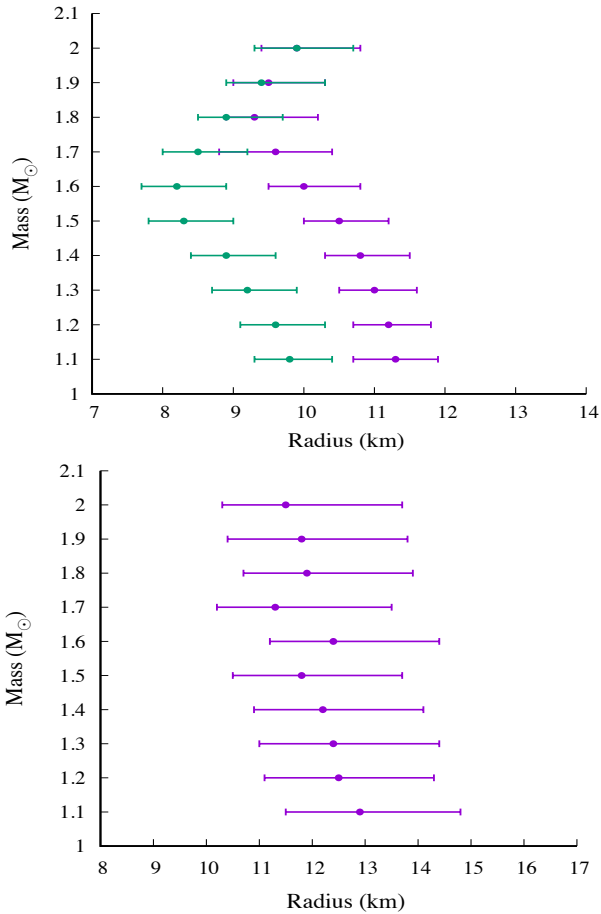


Figure 1. Radius constraints for EXO 0748–676 (top) and Aql X-1 (bottom) for different mass values. As detailed in Section 4.3, for EXO 0748–676 we investigated fits performed over two different energy ranges of 0.3–10 keV (in purple) and 0.5–10 keV (in green). For all other analysis, including that of Aql X-1 shown here, only an energy range of 0.3–10 keV was considered. Error bars reflect 90% confidence levels.

the energy range over which the spectral fits were performed. Fitting the *XMM-Newton* data to a NS atmosphere model, the authors obtained $M = 2.00^{+0.07}_{-0.24} M_{\odot}$ when fitting over 0.3–10 keV and $R = 11.3^{+1.3}_{-1.0}$ km, and $M = 1.5^{+0.4}_{-1.0} M_{\odot}$ and $R = 12.2^{+0.8}_{-3.6}$ km when using a range of 0.5–10 keV (at a confidence level of 90%).

Prompted by these results, we tested if the same effect is seen for *Chandra* data to rule out that it is instrument-specific. Since we performed all our fits initially in the energy range of 0.3–10 keV (see Section 3), we repeated our fits for EXO 0748–676 but now ignoring all data in 0.3–0.5 keV range.

We found that the 0.5–10 keV fits performed for fixed masses resulted in radii of 8–10.5 km for EXO 0748–676, slightly lower than the results of 9–12 km found for spectra fitted in the original energy range (0.3–10 keV). This can be seen in Figure 1 (top), whereas the full details of these fit results are included in Table B1. As can be seen in Table 3, the fit results with the mass and radius both free, also yielded different values than when considering the 0.3–10 keV range, albeit still compatible within the large error bars. We thus also find a lower mass and radius when fitting over 0.5–10 keV rather than over 0.3–10 keV, similar to what Cheng et al. (2017) found when analysing *XMM-Newton* data.

We note that when comparing the fits over the different energy ranges, deviations are also seen in the best-fit values for N_{H} and

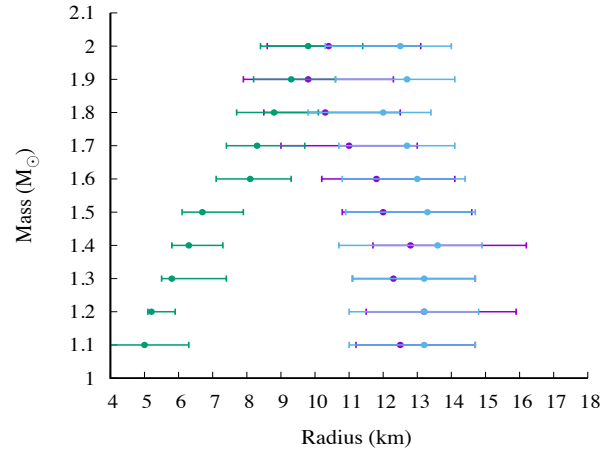


Figure 2. Range of obtained radii for the NS in Aql X-1 for different NS masses. In purple the "Power-Law" sample, in green the "No Power-Law" sample, and in blue the results for the spectra originally assigned to the "No Power-Law" sample after adding a power-law component. In all the performed fits the distance value was kept fixed at 5 kpc. Error bars reflect 90% confidence levels.

kT_{eff} . In Tables 3 and B1 it can be seen that where the outcomes of the fits diverge the most, an analogous difference appears in the N_{H} and kT_{eff} values, being lower for the 0.5–10 keV results than for the 0.3–10 keV ones.

However, as we show in Section 5, *Athena* simulations for EXO 0748–676 result in exactly the same mass and radius pairs for the 0.3–10 and 0.5–10 keV energy range. This suggests that statistics plays an important role in the obtained discrepancy. We note that Aql X-1 was not suitable to perform the same test because of the limited number of counts below ≈ 0.5 keV in the *Chandra* data we considered here (presumably due to its factor ~ 3 higher hydrogen column density than in EXO 0748–676; see Table 1).

4.4 Aql X-1: Dependence of a power-law component

Depending on whether a relevant fraction of the quiescent emission cannot be ascribed to a soft thermal component, we have two different models for describing the observations: a pure NS atmosphere model or a NS atmosphere model with an additional power-law tail. It is interesting then to ask ourselves if both types of spectra are equally suitable for obtaining mass and radius measurements of the NS. Aql X-1 is ideally suited to carry out this comparison; it has been observed multiple times in quiescence (see Table 2) and has a variable spectral shape that is sometimes mostly thermal and at other times contains a significant power-law component that may contribute up to $\sim 80\%$ of the total unabsorbed 0.5–10 keV flux (e.g. Cackett et al. 2011). Based on a simple f-test (see Section 3), every spectrum of Aql X-1 was assigned either to the "No Power-Law" (6 spectra) or the "Power-Law" (8 spectra) sample. The results are summarized in Table 4. If the NS is always uniformly emitting, we would not expect to find differences in the radii obtained for the two different samples.

For the "No Power-Law" sample we find a range of best-fit radii of 5–11.5 km for varying masses, as can be seen in Figure 2 (green). We note that the inferred radius increases with mass and that trends are also observed in the values of N_{H} and kT_{eff} (increasing and decreasing, respectively, for increasing mass values; see Table B3). These trends are not observed for the other Aql X-1 fits,

Source (energy range)	M (M_{\odot})	R (km)	δ_{dist} (km)	N_{H} (10^{21} cm^{-2})	$\log T_{\text{eff}}$	χ^2_{ν} (d.o.f.)
EXO 0748–676 (0.3–10 keV)	$1.65^{+0.11}_{-0.80}$	$10.0^{+2.0}_{-1.0}$	~ 2.5	$0.51^{+0.07}_{-0.09}$	$6.30^{+0.04}_{-0.08}$	1.14(653)
EXO 0748–676 (0.5–10 keV)	$1.40^{+0.13}_{-0.80}$	$8.9^{+1.7}_{-1.0}$	~ 2.5	0.21 ± 0.11	$6.35^{+0.01}_{-0.12}$	1.07(615)
Aql X-1 (0.3–10 keV)	$1.80^{+0.40}_{-0.90}$	$10.2^{+3.2}_{-1.5}$	~ 6	4.10 ± 0.40	$6.29^{+0.04}_{-0.10}$	0.87(540)

Table 3. Simultaneous constraints on the mass and radius of the NSs in EXO 0748–676 and Aql X-1, assuming distances of 7.1 and 5 kpc, respectively. Quoted errors reflect 90% confidence levels. δ_{dist} gives an estimate of the additional error in the radius when the distance uncertainty is taken into account.

ObsID	f -test probability	Assigned Sample
708	0.10	No Power-Law
709	8.8×10^{-5}	Power-Law
710	5.2×10^{-6}	Power-Law
711	3.4×10^{-9}	Power-Law
3484	0.013	No Power-Law
3485	4.9×10^{-9}	Power-Law
3486	6.7×10^{-17}	Power-Law
3487	0.11	No Power-Law
3488	0.056	No Power-Law
3489	1.6×10^{-4}	Power-Law
3490	2.4×10^{-5}	Power-Law
12457	6.4×10^{-5}	Power-Law
12458	1.9×10^{-3}	No Power-Law
12459	1×10^{-3}	No Power-Law

Table 4. Resulting f -tests probability for all observations of Aql X-1 and the resulting sample assignment.

where the N_{H} values tend to the similar values regardless of the chosen mass and the average temperature is positively correlated with M (see Tables B2, B4, and B5). Furthermore, although fits to the individual spectra do not suggest the presence of a significant power-law component in any of them, fitting the whole sample together gives a rather poor fit (see Table B3) and suggest that an NSATMOS-only model might not be the correct description of these data (see below). We carried out a similar analysis for the "Power-Law" sample of Aql X-1, which is presented in Figure 2 as well (purple). We find a wide range of radii from ≈ 8 to 16 km. Notably, this range is overlapping with that of the "No Power-Law" sample only in a small part of this total range. There is thus a mismatch in the results obtained for the two samples. Furthermore, we do not find the same proportionality of R with M that we saw for the sample that we fitted with a NS atmosphere model only, nor the trends exhibited by the kT_{eff} and N_{H} parameters apparent in the "No Power-Law" sample fits. We note that we obtain a power-law index of $\Gamma \approx 1.1 - 1.3$. These fits are presented in Tables B4.

We considered whether an unmodeled power-law component could be the cause of the different results obtained for the two samples, and the bad overall fit for the "No Power-Law" sample. To test this, we repeated the analysis of that sample by fitting the data with a power-law component included. Due to the low number of counts at higher energies ($\gtrsim 3$ keV) in these spectra, we had to fix the power-law component in these fits. We choose to set $\Gamma = 1.2$, which is the value that we obtained for the "Power-Law" sample (see Table B5) and is consistent with previous studies (e.g. Cackett et al. 2011; Campana et al. 2014). As shown in Figure 2 (blue) the best-fit radii for these fits replicate results obtained for the "Power-Law" sample and the overall fit statistic is significantly improved.

As discussed in Section 4.5, we found another peculiar effect for the "No Power Law" sample related to the (lack of a) distance dependence. Taken together, this leads us to believe that in spectra of the sample that were originally earmarked as not containing a significant power-law component, there is in fact an unmodeled

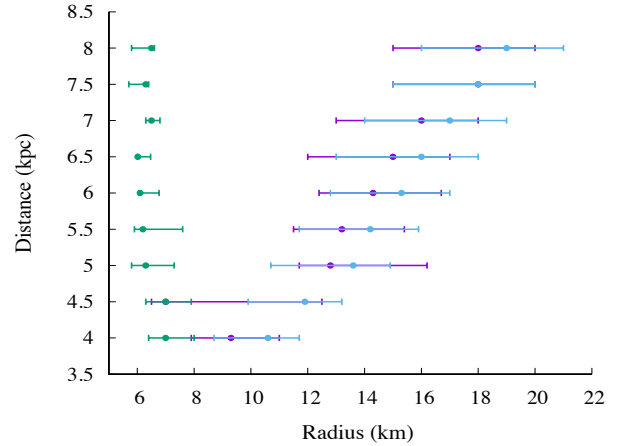


Figure 3. Best-fit radii for Aql X-1 for different values of the distance. In purple, the "Power-law" sample, in green the "No Power-law" sample, and in blue the sample indicated originally indicated as "No Power-law" but now fitted with a power-law spectral component added (with a fixed index of $\Gamma = 1.2$). In all the performed the fits the mass was kept fixed at $1.4 M_{\odot}$. Error bars reflect 90% confidence levels.

hard emission tail that causes unexpected behavior in the fit results. This would suggest that finding a proportionality between the inferred radius and assumed mass can also serve as a test to spot an unmodeled power-law component in the spectra.

Based on our findings above, we performed a final set of fits using all the 14 *Chandra* observations of Aql X-1 with a composite thermal and power-law model, to constrain the mass and radius of this NS. The results of these fits were discussed in Section 4.2 and are listed in Table B2. We note here that the range of inferred radii for the final analysis of all 14 observations, comprised between 10 and 15 km, is only slightly smaller than the initial results from the "Power-Law" sample. Notably, the improvement of simultaneous constraints on mass and radius are not significant, despite that the number of spectra nearly doubled. This is likely due to the fact that the addition of a power-law component increases the number of free fit parameters and the level of degeneracy. Nevertheless, the presence of a hard emission tail in itself does not necessarily limit the constraints that can be obtained for the NS parameters. As we show in Section 5, very high-quality spectra such as can be obtained with *Athena*, have the potential to yield accurate mass and radius measurements even when the quiescent spectrum contains a significant hard emission tail.

4.5 The influence of the distance uncertainty

The uncertainty about the distance of a source is one of the main issues of this technique. If the distance is not known accurately, a range of distance values can be chosen for the analysis and this will bias the results. Since the observed thermal flux is proportional to $(R/D)^2$, a larger distance should return a larger NS radius. To

illustrate the magnitude of this bias we launched multiple fits for EXO 0748–676 and Aql X-1, in which the distances were fixed to different values within the allowed range for each source. These ranges are 5.9–8.3 kpc for EXO 0748–676 (Section A4) and 4–8 kpc for Aql X-1 (Section A6). In all these fits we fixed $M = 1.4 M_{\odot}$ to reduce the number of degrees of freedom.

The expected proportionality relation between the NS radius and distance is indeed recovered for EXO 0748–676. The best-fit radius goes from ~ 8.5 –9.5 km at a distance of 6.1 kpc to $R \sim 12$ –13 km at the other end of the distance confidence range (see Table B6). This shows that allowing the full distance range gives an additional uncertainty of $\delta_{\text{dist}} \sim 2.5$ km for the NS radius. For Aql X-1, we performed fits with different distances for both the “Power-law” and “No Power-law” sample (see Section 4.4 and Table 4). For the former we observe the same expected behavior as for EXO 0748–676, where the inferred radius increases with assumed distance (see Figure 3, purple). We find radii between 8–11 km when using 4 kpc and 16–20 km when using 8 kpc (see Table B3). Accounting for the distance uncertainty thus results in an additional error $\delta_{\text{dist}} \sim 6$ km on the best-fit radius.

For the Aql X-1 spectra that we identified as not requiring a power-law spectral component, however, we do not find the expected proportionality between R and D . In Figure 3 (green) it can be seen that for this selection of spectra the obtained radius does not depend on the assumed distance. In addition, the obtained radii are unphysically small for a NS. Failure to recover the expected correlation may indicate that the data are not modeled correctly, as is also suggested by the poor χ^2 fit values obtained when the entire sample is modeled simultaneously (see Table B3). To test this, we repeated the spectral fits of the original “No Power Law” after including a power-law component with a fixed index of $\Gamma = 1.2$ (see Section 4.4). Indeed, the proportionality between R and D is then seen (Figure 3 blue; see also Table B3), and is similar to the results obtained for the original “Power Law” sample. This seems to suggest again that despite the low f-test probability for the individual spectra, there might be a power-law tail contained in all these spectra after all.

To conclude this part of our analysis, we performed one last series of fits to probe the distance bias for the all-inclusive sample, i.e. comprising all 14 *Chandra* observations, fitted to a composite model that includes a power-law component. With radius estimates fluctuating from 9–12 to 16–20 km from one end to the other of the distance range, it is clear that the expected $D - R$ proportionality is again maintained (see Table B2). Our results on Aql X-1 indicate that failure to recover the expected D dependency may also serve as a test to see if there is an unmodeled power-law component in the data.

5 ATHENA SIMULATIONS

Not surprisingly, our analysis shows that good statistics is key to obtain NS mass and radius constraints for field qLMXBs. It is then interesting to explore if such constraints can be improved with new instrumentation and if this can also help to lift certain biases. To this end we performed simulations for ESA’s *Athena* mission, which is currently scheduled for launch in the late 2020s (Barcons et al. 2015). Its large collective area at soft X-ray energies is expected to be very useful for obtaining NS mass and radius constraints from studying their quiescent thermal X-ray emission. Performing these simulations thus allows us to probe if and how much the limits of this technique depend on the quality of our spectra.

All simulations were performed using the XSPEC command FAKEIT, which builds a synthetic spectrum based on a given model. For these simulations we used currently available theoretical *rmf* and *arf* of the Wide Field Imager (WFI), including a simulated background, and assumed a modest exposure time of 50 ks.⁴ The simulated spectra were rebinned into channels with a minimum of 20 counts per bin and then we performed the same analysis carried out for the *Chandra* data on these synthetic *Athena* data.

In our current work, five of the seven selected sources did not give satisfactory results mainly because of the low statistics (see Section 4.1). Since 4U 1608–52 is a source for which different techniques can in principle be employed to lead to M and R constraints (see Section A7), making this a promising target, we simulated the quiescent spectrum of this particular source. Recall that the single *Chandra* observation available for 4U 1608–52 (23 ks) did not provide meaningful constraints on the NS parameters (Section 4.1), presumably due to the combined effect of a relatively high absorption column density (reducing the number of photons at low energies) and the presence of a power-law spectral component (increasing the level of degeneracy with the thermal component).

The results of our *Athena* simulations for 4U 1608–52 are shown in Figure 4, where they are directly compared with the currently available *Chandra* data. Leveraging the enhanced statistics of the simulated data we tried to constrain both mass and radius. Using a composite thermal and power-law model, we obtain best-fit values for the mass and radius of $M = 1.735 \pm 0.003 M_{\odot}$ and $R = 10.91^{+0.14}_{-0.19}$ km. These simulations demonstrate that very accurate constraints on the mass and radius can be obtained from quiescent spectra with significantly improved statistics (at a level of less than a few percent if the distance is well known), even if the absorption column density is relatively high and if there is a power-law component present. When taking into account the full distance range estimated for 4U 1608–52, an additional uncertainty of $\delta_{\text{dist}} \sim 2$ km on the radius is obtained.

We also tested if the dependence on the energy range would remain an issue if better quality data is available. To this end we simulated an *Athena* spectrum for EXO 0748–676 based on the best-fit values of our fits with both mass and radius free (see Table 3) in the range 0.3–10 keV, and then fitted this spectrum with the model TBABS×NSATMOS. We launched one fit using the energy range 0.3–10 keV and another one on the energy range 0.5–10 keV, to check if the same energy range bias observed in *Chandra* (and *XMM-Newton*) spectra may still be an issue dealing with *Athena* data. The two results are perfectly consistent with the input values for the simulation and with each other: we obtain $M = 1.641^{+0.011}_{-0.080} M_{\odot}$ and $R = 10.06^{+0.05}_{-0.06}$ km when fitting over the 0.3–10 keV range and $M = 1.646^{+0.016}_{-0.013} M_{\odot}$ and $R = 10.02^{+0.11}_{-0.09}$ km when considering 0.5–10 keV instead. This suggests that the dependence on the energy range is something that may depend only on the quality of the spectral data. Due to the lack of a power-law component, the radius can be measured even more accurately than for 4U 1608–52, with $\sim 1\%$ errors, if the distance were known accurately. Accounting for the distance uncertainty of EXO 0748–676 yields and error of $\delta_{\text{dist}} \sim 2.5$ km on the NS radius.

We note that these simulations are based on current assumptions for e.g. coating efficiency, coating thickness versus annu-

⁴ Specifically, we used *athena_wfi_1190_onaxis_w_filter_v20150326.rsp* (*rmf*), *athena_wfi_1190_onaxis_w_filter_v20150326.arf* (*arf*) and *athena_wfi_1469_bkgd_sum_psf_onaxis_w_filter_20150327.pha* (*bg*), taken from <https://www.cosmos.esa.int/web/athena/resources-by-esa>

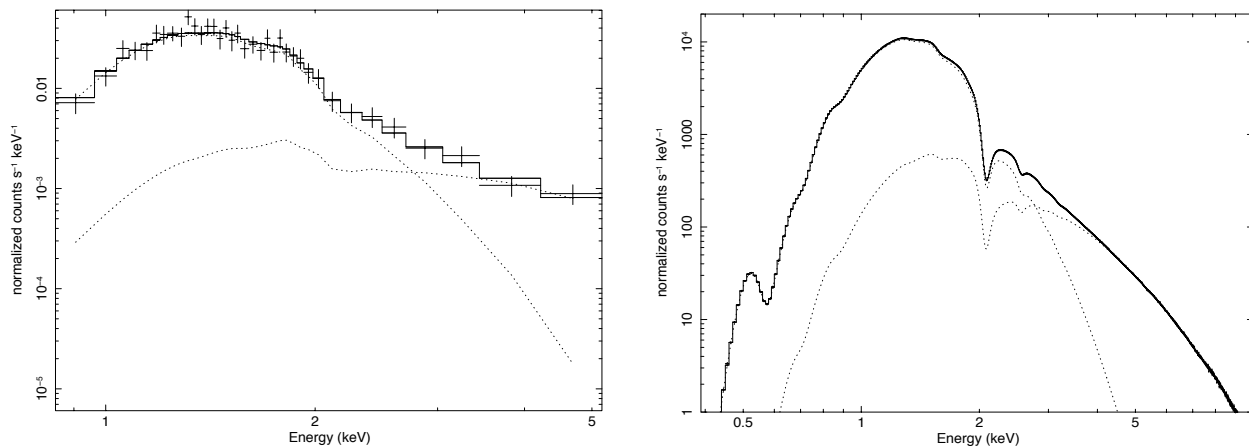


Figure 4. Quiescent X-ray spectra of 4U 1608–52. Left: Observed *Chandra*/ACIS-S spectrum (exposure time of 23 ks). Right: Simulated *Athena*/WFI spectrum based on the model used to fit the *Chandra* data (exposure time of 50 ks). The solid curves indicate fits to a composite model comprised of a NS atmosphere (dominating the emission at energies below ~ 3 keV) and a hard power-law tail, which are indicated by the dotted curves.

lus, roughness, etc., for the *Athena*/WFC design and are presented merely to illustrate the advances brought by higher quality data. The results from the simulations should of course not be taken at face value.

6 SUMMARY AND OUTLOOK

In this work we analyzed *Chandra* spectra of seven quiescent LMXBs residing in the Galactic Plane. Our main aim was to probe to what extent such objects can be used to constrain the radius (and mass) of the NS, and in particular to test the robustness of such results against several biases this method is subject to. The motivation for this work is that field LMXBs have some advantages over globular cluster sources, mostly used for this type of analysis so far, particularly if their distances could be more accurately determined (e.g. with *Gaia*).

We found that for only two of the sources in our sample, EXO 0748–676 and Aql X-1, the quality of the spectral data was sufficient to obtain some constraints on the NS radius and mass. For the other five NS LMXBs no such results could be obtained due to limited statistics ($\lesssim 3000$ counts in a spectrum), which is in part due to factors like the interstellar absorption, and/or the presence of a power-law spectral component.

For EXO 0748–676 and Aql X-1, which both have multiple *Chandra* quiescence observations and a relatively low N_{H} , we found NS radii of $R < 15$ and $R < 19$ km, respectively (90% confidence ranges, fitting the data between 0.3–10 keV and assuming a NS mass of $1.4 M_{\odot}$, taking into account the full available distance range). Although these results depend on the distance and the energy range for spectral fitting, we can consider these values as upper limits for the NS radius, because these are valid under the various parameter ranges that were probed. In principle for both sources the mass and radius could be constrained simultaneously from the spectral fits, albeit with large errors (see Table 3).

The NS parameters can be much less well constrained for Aql X-1 than for EXO 0748–676, which is likely due to the higher statistics of the latter (because of a combination of lower absorption column density and absence of a power-law spectral component) and the greater distance uncertainty in the former.

Using the *Chandra* data of EXO 0748–676, we investigated

the dependence of the inferred NS parameters on the energy range over which the spectral fits are performed. For fits performed using data between 0.5–10 keV we found systematically lower radii (and masses) than for fits that extended to a lower energy of 0.3 keV. This effect was also spotted when using *XMM-Newton* data of this source (Cheng et al. 2017). This indicates that the chosen range for spectral fitting biases the obtained NS radius and mass. However, *Athena* simulations that we performed for EXO 0748–676 return no such energy dependence, indicating that this bias can possibly be lifted with increased statistics.

Using the *Chandra* data of Aql X-1, we investigated the effect of a power-law spectral component in the data. Based on the simple and often used f-test, we initially divided the 14 observations for this source as either being a pure NS atmosphere, or requiring an additional power-law emission tail. For the former sample we found a general bad agreement between data and model, witnessed by values of $\chi^2_{\nu} \sim 1.5$, and the arising of on the one hand an unexpected correlation between the obtained radius and assumed mass, and on the other hand the lack of the expected correlation between the inferred radius and assumed distance. Trends in the values for N_{H} and the average effective temperature obtained by the fits were observed as well. All these effects disappeared when a power-law component was added to the spectra that were originally diagnosed as likely being pure NS atmospheres. This suggests that a hard emission tail is hidden in those spectra and by not modeling it, this peculiar behavior is observed. Testing the mass and distance dependence of the NS radii inferred from spectral fits may thus both serve as simple tests to see if there might be an unmodeled power-law component present in the data.

We performed *Athena* simulations for the NS LMXB 4U 1608–52 to probe the advances that may be brought by future instrumentation. For this source we could not obtain meaningful results using the existing *Chandra* data, presumably due to its relatively high column density and the presence of a hard emission tail in the quiescent spectrum. We found that with highly increased statistics the presence of a power-law spectral component does not hamper obtaining accurate constraints on the NS parameters. Indeed, the mass and radius can in principle be very accurately constrained simultaneously with *Athena*, provided that the distance towards the source is well known.

Despite the advances expected to be brought by future mis-

sions, an important caveat is, as discussed in Section 1, that the presence of a power-law component in the spectrum might be interpreted as the signature of residual accretion. As argued in Wijnands et al. (2015), a power-law component that contributes $\sim 50\%$ to total unabsorbed 0.5–10 keV flux very likely originates from accretion, whereas a much lower power-law contribution could have a different origin. The presence of low-level accretion can hamper reliable radius measurements. For instance, low-level accretion could keep the metal abundance in the atmosphere high enough to soften the spectrum, causing an overestimate of the NS radius (Rutledge et al. 2002b). On the other hand, if accretion is ongoing and concentrated onto a fraction of the NS, the inferred radius may be underestimated the true one. Fortunately, there are several field LMXBs (e.g. EXO 0748–676, MXB 1659–298 and KS 1731–260 studied in this work) that have spectra fitted well by NS atmosphere models without showing evidence for an additional power-law component (or any other signs of low-level accretion such as irregular variability).

Uncertainties in the source distance results in a well-known bias in the obtained radius. This problem is more severe for field LMXBs as their distances are often less well constrained than for the ones located in globular clusters. However, new and more precise distance measurements may become available in the near future from *GAIA* (Global Astrometric Interferometer for Astrophysics; Gaia Collaboration et al. 2016). This ESA space observatory has been measuring, since 2013, parallax distances of millions of stars, visible in the optical band, with an unprecedented precision.⁵ One in three LMXBs have a known optical counterpart (Liu et al. 2007), and more accurate distances may be obtained with *Gaia* for some field NS LMXBs. This can strongly reduce the uncertainties on their measured radii (and masses).

The advances brought by sensitive X-ray detectors with a high collective area, such as *Athena*, might provide good prospects for obtaining reliable NS radius (and mass) constraints for field LMXBs using their quiescent thermal X-ray emission. Such studies are particularly promising for sources for which more accurate distances can be determined, and that have a low hydrogen column density and small or absent contribution from a hard emission tail in their quiescent spectra. Furthermore, for some of these sources other measurements may be obtained, such as independent R and M estimates from thermonuclear X-ray bursts, dynamical mass measurements for sources that have bright optical counterparts, or indirect constraints from the accretion flow properties (reflection features and QPOs). Some field LMXBs, e.g. Aql X-1 and 4U 1608–52, meet several of these requirements.

ACKNOWLEDGEMENTS

The authors are grateful to the anonymous referee for a thoughtful report that helped improve the clarity of this work. AM was partly supported by an "ERASMUS+ for traineeship" grant and partly by the NewCompStar network, COST Action MP1304. AM thanks the hospitality of the Anton Pannekoek Institute for Astronomy in Amsterdam, where most of this research was carried out. ND is supported by a Vidi grant awarded by the Netherlands organization for scientific research (NWO). RW is supported by Top-1 grant from NWO. The authors acknowledge financial contribution from the agreement ASI-INAF I/037/12/0, as well as fruitful discussion with

the international team "The disk-magnetosphere interaction around transitional millisecond pulsars" at the International Space Science Institute, Bern. This work is partially supported by the HERMES Project, financed by the Italian Space Agency (ASI) Agreement n. 2016/13 U.O

REFERENCES

- Anders E., Grevesse N., 1989, *Geochimica Cosmochimica Acta*, 53, 197
 Antoniadis J., et al., 2013, *Science*, 340, 448
 Asai K., Dotani T., Mitsuda K., Hoshi R., Vaughan B., Tanaka Y., Inoue H., 1996, *PASJ*, 48, 257
 Asai K., Dotani T., Hoshi R., Tanaka Y., Robinson C., Terada K., 1998, *PASJ*, 50, 611
 Bahramian A., et al., 2014, *ApJ*, 780, 127
 Bahramian A., Heinke C. O., Degenaar N., Chomiuk L., Wijnands R., Strader J., Ho W. C. G., Pooley D., 2015, *MNRAS*, 452, 3475
 Barcons X., Nandra K., Barret D., den Herder J.-W., Fabian A. C., Piro L., Watson M. G., the Athena Team 2015, in *Journal of Physics Conference Series*. p. 012008, doi:10.1088/1742-6596/610/1/012008
 Barret D., Olive J.-F., Miller M. C., 2006, *MNRAS*, 370, 1140
 Bassa C. G., Jonker P. G., Steeghs D., Torres M. A. P., 2009, *MNRAS*, 399, 2055
 Berger M., et al., 1996, *ApJ*, 469, L13
 Bernardini F., Cackett E. M., Brown E. F., D'Angelo C., Degenaar N., Miller J. M., Reynolds M., Wijnands R., 2013, *MNRAS*, 436, 2465
 Bhattacharyya S., 2010, *Advances in Space Research*, 45, 949
 Bogdanov S., Heinke C. O., Özel F., Güver T., 2016, *ApJ*, 831, 184
 Brown E. F., Bildsten L., 1998, in Paul J., Montmerle T., Aubourg E., eds, *19th Texas Symposium on Relativistic Astrophysics and Cosmology*.
 Cackett E. M., Wijnands R., Linares M., Miller J. M., Homan J., Lewin W. H. G., 2006, *MNRAS*, 372, 479
 Cackett E. M., Wijnands R., Miller J. M., Brown E. F., Degenaar N., 2008, *ApJ*, 687, L87
 Cackett E. M., Brown E. F., Miller J. M., Wijnands R., 2010a, *ApJ*, 720, 1325
 Cackett E. M., Brown E. F., Cumming A., Degenaar N., Miller J. M., Wijnands R., 2010b, *ApJ*, 722, L137
 Cackett E. M., Fridriksson J. K., Homan J., Miller J. M., Wijnands R., 2011, *MNRAS*, 414, 3006
 Cackett E. M., Brown E. F., Degenaar N., Miller J. M., Reynolds M., Wijnands R., 2013a, *MNRAS*, 433, 1362
 Cackett E. M., Brown E. F., Cumming A., Degenaar N., Fridriksson J. K., Homan J., Miller J. M., Wijnands R., 2013b, *ApJ*, 774, 131
 Callanan P. J., Filippenko A. V., Garcia M. R., 1999, *IAU Circ.*, 7086
 Campana S., Stella L., 2003, *ApJ*, 597, 474
 Campana S., Mereghetti S., Stella L., Colpi M., 1997, *A&A*, 324, 941
 Campana S., Colpi M., Mereghetti S., Stella L., Tavani M., 1998, *A&ARv*, 8, 279
 Campana S., Stella L., Mereghetti S., Cremonesi D., 2000, *A&A*, 358, 583
 Campana S., et al., 2002, *ApJ*, 575, L15
 Campana S., Coti Zelati F., D'Avanzo P., 2013, *MNRAS*, 432, 1695
 Campana S., Brivio F., Degenaar N., Mereghetti S., Wijnands R., D'Avanzo P., Israel G. L., Stella L., 2014, *MNRAS*, 441, 1984
 Casares J., González Hernández J. I., Israelian G., Reboloto R., 2010, *MNRAS*, 401, 2517
 Casella P., Altamirano D., Patruno A., Wijnands R., van der Klis M., 2008, *ApJ*, 674, L41
 Catuneanu A., Heinke C. O., Sivakoff G. R., Ho W. C. G., Servillat M., 2013, *ApJ*, 764, 145
 Chakrabarty D., et al., 2014, *ApJ*, 797, 92
 Cheng Z., Méndez M., Díaz-Trigo M., Costantini E., 2017, *MNRAS*, 471, 2605
 Chevalier C., Ilovaisky S. A., van Paradijs J., Pedersen H., van der Klis M., 1989, *A&A*, 210, 114
 Chiang C.-Y., et al., 2016, *ApJ*, 821, 105

⁵ The expected precision is 1% for nearest stars to 10% for sources close to the Galactic Center, about 10 kpc from the Earth.

- Cominsky L. R., Wood K. S., 1984, *ApJ*, 283, 765
Cominsky L. R., Wood K. S., 1989, *ApJ*, 337, 485
Conner J. P., Evans W. D., Belian R. D., 1969, *ApJ*, 157, L157
Cornelisse R., Wijnands R., Homan J., 2007, *MNRAS*, 380, 1637
Coti Zelati F., Campana S., D'Avanzo P., Melandri A., 2014, *MNRAS*, 438, 2634
D'Angelo C. R., Fridriksson J. K., Messenger C., Patruno A., 2015, *MNRAS*, 449, 2803
D'Avanzo P., Campana S., Casares J., Israel G. L., Covino S., Charles P. A., Stella L., 2005, *A&A*, 444, 905
Degenaar N., Wijnands R., 2012, *MNRAS*, 422, 581
Degenaar N., et al., 2009, *MNRAS*, 396, L26
Degenaar N., et al., 2011, *MNRAS*, 412, 1409
Degenaar N., Wijnands R., Cackett E. M., Homan J., in't Zand J. J. M., Kuulkers E., Maccarone T. J., van der Klis M., 2012a, *A&A*, 545, A49
Degenaar N., Patruno A., Wijnands R., 2012b, *ApJ*, 756, 148
Degenaar N., et al., 2014, *ApJ*, 791, 47
Degenaar N., Miller J. M., Chakrabarty D., Harrison F. A., Kara E., Fabian A. C., 2015, *MNRAS*, 451, L85
Degenaar N., Ootes L. S., Reynolds M. T., Wijnands R., Page D., 2017, *MNRAS*, 465, L10
Degenaar N., et al., 2018, *Space Sci. Rev.*, 214, 15
Demorest P. B., Pennucci T., Ransom S. M., Roberts M. S. E., Hessels J. W. T., 2010, *Nature*, 467, 1081
Di Salvo T., Burderi L., 2003, *A&A*, 397, 723
Díaz Trigo M., Boirin L., Costantini E., Méndez M., Parmar A., 2011, *A&A*, 528, A150
Ebisuzaki T., 1987, *PASJ*, 39, 287
Elebert P., et al., 2009, *MNRAS*, 395, 884
Elshamouty K. G., Heinke C. O., Morsink S. M., Bogdanov S., Stevens A. L., 2016, *ApJ*, 826, 162
Elsner R. F., Lamb F. K., 1977, *ApJ*, 215, 897
Fonseca E., et al., 2016, *ApJ*, 832, 167
Fortin M., Avancini S. S., Providência C., Vidiña I., 2017, *Phys. Rev. C*, 95, 065803
Fridriksson J. K., et al., 2010, *ApJ*, 714, 270
Fridriksson J. K., et al., 2011a, *ApJ*, 736, 162
Fridriksson J. K., et al., 2011b, *ApJ*, 736, 162
Friedman H., Byram E. T., Chubb T. A., 1967, *Science*, 156, 374
Fujimoto M. Y., Gottwald M., 1989, *MNRAS*, 236, 545
Gaia Collaboration et al., 2016, *A&A*, 595, A1
Galloway D. K., Muno M. P., Hartman J. M., Psaltis D., Chakrabarty D., 2008a, *ApJS*, 179, 360
Galloway D., Özel F., Psaltis D., 2008b, *MNRAS*, 387, 268
Galloway D., Lin J., Chakrabarty D., Hartman J. M., 2010, in *AAS/High Energy Astrophysics Division #11*. p. 728
Goodman J., Weare J., 2010, *Communications in Applied Mathematics and Computational Science*, Vol.~5, No.~1, p.~65-80, 2010, 5, 65
Gottwald M., Stella L., White N. E., Barr P., 1987, *MNRAS*, 229, 395
Guillot S., Servillat M., Webb N. A., Rutledge R. E., 2013, *ApJ*, 772, 7
Güver T., Özel F., Cabrera-Lavers A., Wroblewski P., 2010, *ApJ*, 712, 964
Haakonsen C. B., Turner M. L., Tacik N. A., Rutledge R. E., 2012, *ApJ*, 749, 52
Haensel P., Zdenik J. L., 2003, *A&A*, 404, L33
Hebeler K., Lattimer J. M., Pethick C. J., Schwenk A., 2013, *ApJ*, 773, 11
Heinke C. O., 2013, in *Journal of Physics Conference Series*. p. 012001 ([arXiv:1303.0317](https://arxiv.org/abs/1303.0317)), doi:10.1088/1742-6596/432/1/012001
Heinke C. O., Grindlay J. E., Lloyd D. A., Edmonds P. D., 2003a, *ApJ*, 588, 452
Heinke C. O., Grindlay J. E., Lugger P. M., Cohn H. N., Edmonds P. D., Lloyd D. A., Cool A. M., 2003b, *ApJ*, 598, 501
Heinke C. O., Rybicki G. B., Narayan R., Grindlay J. E., 2006, *ApJ*, 644, 1090
Heinke C. O., Jonker P. G., Wijnands R., Taam R. E., 2007, *ApJ*, 660, 1424
Heinke C. O., Jonker P. G., Wijnands R., Deloye C. J., Taam R. E., 2009, *ApJ*, 691, 1035
Heinke C. O., et al., 2014, *MNRAS*, 444, 443
Ho W. C. G., Heinke C. O., 2009, *Nature*, 462, 71
Homan J., et al., 2007, *ApJ*, 656, 420
Homan J., Fridriksson J. K., Wijnands R., Cackett E. M., Degenaar N., Linares M., Lin D., Remillard R. A., 2014, *ApJ*, 795, 131
Ikhsanov N. R., 2001, *A&A*, 375, 944
Jonker P. G., Nelemans G., 2004, *MNRAS*, 354, 355
Jonker P. G., Méndez M., van der Klis M., 2000, *ApJ*, 540, L29
Jonker P. G., Galloway D. K., McClintock J. E., Buxton M., Garcia M., Murray S., 2004, *MNRAS*, 354, 666
Jonker P. G., Bassa C. G., Wachter S., 2007a, *MNRAS*, 377, 1295
Jonker P. G., Steeghs D., Chakrabarty D., Juett A. M., 2007b, *ApJ*, 665, L147
Kajava J. J. E., et al., 2014, *MNRAS*, 445, 4218
Kalberla P. M. W., Burton W. B., Hartmann D., Arnal E. M., Bajaja E., Morras R., Pöppel W. G. L., 2005, *A&A*, 440, 775
Kaluzienski L. J., Holt S. S., Boldt E. A., Serlemitsos P. J., 1977, *Nature*, 265, 606
Kaluzienski L. J., Holt S. S., Swank J. H., 1980, *ApJ*, 241, 779
Kitamoto S., Tsunemi H., Miyamoto S., Roussel-Dupre D., 1993, *ApJ*, 403, 315
Koyama K., et al., 1981, *ApJ*, 247, L27
Lattimer J. M., 2012, *Annual Review of Nuclear and Particle Science*, 62, 485
Leahy D. A., Morsink S. M., Cadeau C., 2008, *ApJ*, 672, 1119
Lewin W. H. G., Hoffman J. A., Doty J., Liller W., 1976, *IAU Circ.*, 2994
Lewin W. H. G., van Paradijs J., Taam R. E., 1993, *Space Sci. Rev.*, 62, 223
Li Z., Falanga M., Chen L., Qu J., Xu R., 2017, *ApJ*, 845, 8
Lii P. S., Romanova M. M., Ustyugova G. V., Koldoba A. V., Lovelace R. V. E., 2014, *MNRAS*, 441, 86
Lin D., Altamirano D., Homan J., Remillard R. A., Wijnands R., Belloni T., 2009, *ApJ*, 699, 60
Liu Q. Z., van Paradijs J., van den Heuvel E. P. J., 2007, *A&A*, 469, 807
Lo K. H., Miller M. C., Bhattacharyya S., Lamb F. K., 2013, *ApJ*, 776, 19
Lochner J. C., Roussel-Dupre D., 1994, *ApJ*, 435, 840
Ludlam R. M., et al., 2017, *ApJ*, 836, 140
Martínez J. G., et al., 2015, *ApJ*, 812, 143
Mata Sánchez D., Muñoz-Darias T., Casares J., Jiménez-Ibarra F., 2017, *MNRAS*, 464, L41
Matranga M., Di Salvo T., Iaria R., Gambino A. F., Burderi L., Riggio A., Sanna A., 2017, *A&A*, 600, A24
McClintock J. E., Remillard R. A., 1990, *ApJ*, 350, 386
Méndez M., et al., 1998, *ApJ*, 494, L65
Merritt R. L., et al., 2016, *ApJ*, 833, 186
Meyer-Hofmeister E., 2004, *A&A*, 423, 321
Miller M. C., Lamb F. K., 2015, *ApJ*, 808, 31
Miller M. C., Lamb F. K., 2016, *European Physical Journal A*, 52, 63
Miller M. C., Lamb F. K., Psaltis D., 1998, *ApJ*, 508, 791
Miller J. M., et al., 2013, *ApJ*, 779, L2
Muñoz-Darias T., Casares J., O'Brien K., Steeghs D., Martínez-Pais I. G., Cornelisse R., Charles P. A., 2009, *MNRAS*, 394, L136
Muno M. P., Fox D. W., Morgan E. H., Bildsten L., 2000a, *ApJ*, 542, 1016
Muno M. P., Fox D. W., Morgan E. H., Bildsten L., 2000b, *ApJ*, 542, 1016
Muno M. P., Chakrabarty D., Galloway D. K., Savov P., 2001, *ApJ*, 553, L157
Murakami T., et al., 1980, *ApJ*, 240, L143
Nath N. R., Strohmayer T. E., Swank J. H., 2002, *ApJ*, 564, 353
Nättilä J., Suleimanov V. F., Kajava J. J. E., Poutanen J., 2015, *A&A*, 581, A83
Nättilä J., Steiner A. W., Kajava J. J. E., Suleimanov V. F., Poutanen J., 2016, *A&A*, 591, A25
Oosterbroek T., Parmar A. N., Sidoli L., in't Zand J. J. M., Heise J., 2001, *A&A*, 376, 532
Ootes L. S., Wijnands R., Page D., Degenaar N., 2018, preprint, ([arXiv:1802.06081](https://arxiv.org/abs/1802.06081))
Orosz J. A., Kuulkers E., 1999, *MNRAS*, 305, 132
Özel F., 2006, *Nature*, 441, 1115
Özel F., Freire P., 2016, *ARA&A*, 54, 401
Özel F., Psaltis D., Narayan R., Santos Villarreal A., 2012, *ApJ*, 757, 55
Parikh A. S., et al., 2017a, *MNRAS*, 466, 4074

- Parikh A. S., et al., 2017b, *ApJ*, 851, L28
- Parmar A. N., Gottwald M., Haberl F., Giommi P., White N. E., 1985, in Burke W. R., ed., *ESA Special Publication Vol. 236, Recent Results on Cataclysmic Variables. The Importance of IUE and Exosat Results on Cataclysmic Variables and Low-Mass X-Ray Binaries.*
- Pavlov G. G., Zavlin V. E., 1997, *ApJ*, 490, L91
- Poutanen J., Gierliński M., 2003, *MNRAS*, 343, 1301
- Poutanen J., Nättilä J., Kajava J. J. E., Latvala O.-M., Galloway D. K., Kuulkers E., Suleimanov V. F., 2014, *MNRAS*, 442, 3777
- Revnivtsev M., Churazov E., Gilfanov M., Sunyaev R., 2001, *A&A*, 372, 138
- Rouco Escorial A., Bak Nielsen A. S., Wijnands R., Cavecchi Y., Degenaar N., Patruno A., 2017, *MNRAS*, 472, 1802
- Rutledge R. E., Bildsten L., Brown E. F., Pavlov G. G., Zavlin V. E., 1999, *ApJ*, 514, 945
- Rutledge R. E., Bildsten L., Brown E. F., Pavlov G. G., Zavlin V. E., 2001a, *ApJ*, 551, 921
- Rutledge R. E., Bildsten L., Brown E. F., Pavlov G. G., Zavlin V. E., 2001b, *ApJ*, 559, 1054
- Rutledge R., Bildsten L., Brown E., Pavlov G., Zavlin V., 2002a, *ApJ*, 577, 346
- Rutledge R. E., Bildsten L., Brown E. F., Pavlov G. G., Zavlin V. E., Ushomirsky G., 2002b, *ApJ*, 580, 413
- Servillat M., Heinke C. O., Ho W. C. G., Grindlay J. E., Hong J., van den Berg M., Bogdanov S., 2012, *MNRAS*, 423, 1556
- Shahbaz T., Naylor T., Charles P. A., 1993, *MNRAS*, 265, 655
- Shahbaz T., Charles P. A., King A. R., 1998, *MNRAS*, 301, 382
- Smith D., Morgan E., Bradt H., 1997, *ApJ*, 479, L137
- Steiner A. W., Lattimer J. M., Brown E. F., 2013, *ApJ*, 765, L5
- Steiner A. W., Heinke C. O., Bogdanov S., Li C. K., Ho W. C. G., Bahramian A., Han S., 2018, *MNRAS*, 476, 421
- Stiele H., Yu W., Kong A. K. H., 2016, *ApJ*, 831, 34
- Strohmayer T. E., Zhang W., Swank J. H., Smale A., Titarchuk L., Day C., Lee U., 1996, *ApJ*, 469, L9
- Suleimanov V., Poutanen J., Werner K., 2011, *A&A*, 527, A139
- Sunyaev R. A., et al., 1989, in Hunt J., Battrick B., eds, *ESA Special Publication Vol. 296, Two Topics in X-Ray Astronomy, Volume 1: X Ray Binaries. Volume 2: AGN and the X Ray Background.*
- Tananbaum H., Chaisson L. J., Forman W., Jones C., Matilsky T. A., 1976, *ApJ*, 209, L125
- Tomsick J. A., Gelino D. M., Halpern J. P., Kaaret P., 2004, *ApJ*, 610, 933
- Torres M. A. P., Casares J., Martínez-Pais I. G., Charles P. A., 2002, *MNRAS*, 334, 233
- Verbunt F., Belloni T., Johnston H., van der Klis M., Lewin W., 1994, *A&A*, 285, 903
- Verner D. A., Ferland G. J., Korista K. T., Yakovlev D. G., 1996, *ApJ*, 465, 487
- Wachter S., Hoard D. W., Bailyn C. D., Corbel S., Kaaret P., 2002, *ApJ*, 568, 901
- Wang Z., Breton R. P., Heinke C. O., Deloye C. J., Zhong J., 2013, *ApJ*, 765, 151
- Waterhouse A. C., Degenaar N., Wijnands R., Brown E. F., Miller J. M., Altamirano D., Linares M., 2016, *MNRAS*, 456, 4001
- Watts A., et al., 2015, *Advancing Astrophysics with the Square Kilometre Array*, p. 43
- Watts A. L., et al., 2016, *Reviews of Modern Physics*, 88, 021001
- Webb N. A., Barret D., 2007, *ApJ*, 671, 727
- Wijnands R., Strohmayer T., Franco L. M., 2001a, *ApJ*, 549, L71
- Wijnands R., Miller J., Markwardt C., Lewin W., van der Klis M., 2001b, *ApJ*, 560, L159
- Wijnands R., Guainazzi M., van der Klis M., Méndez M., 2002, *ApJ*, 573, L45
- Wijnands R., Nowak M., Miller J. M., Homan J., Wachter S., Lewin W. H. G., 2003, *ApJ*, 594, 952
- Wijnands R., Homan J., Miller J. M., Lewin W. H. G., 2004, *ApJ*, 606, L61
- Wijnands R., Degenaar N., Armas Padilla M., Altamirano D., Cavecchi Y., Linares M., Bahramian A., Heinke C. O., 2015, *MNRAS*, 454, 1371
- Wijnands R., Degenaar N., Page D., 2017, *Journal of Astrophysics and Astronomy*, 38, 49
- Wilms J., Allen A., McCray R., 2000, *ApJ*, 542, 914
- Wolff M. T., Ray P. S., Wood K. S., Hertz P. L., 2009, *ApJS*, 183, 156
- Wu Y. X., Yu W., Li T. P., Maccarone T. J., Li X. D., 2010, *ApJ*, 718, 620
- Zamfir M., Cumming A., Galloway D. K., 2012, *ApJ*, 749, 69
- Zavlin V. E., Pavlov G. G., Shibano Y. A., 1996, *A&A*, 315, 141
- Zhang S. N., Yu W., Zhang W., 1998, *ApJ*, 494, L71
- Zurita C., Kuulkers E., Bandyopadhyay R. M., Cackett E. M., Groot P. J., Orosz J. A., Torres M. A. P., Wijnands R., 2010, *A&A*, 512, A26
- Šimon V., 2004, *A&A*, 418, 617
- van Paradijs J., Lewin W. H. G., 1990, in Kundt W., ed., *NATO Advanced Science Institutes (ASI) Series C Vol. 300, NATO Advanced Science Institutes (ASI) Series C. p. 239*
- van Paradijs J., Verbunt F., Shafer R., Arnaud K., 1987, *A&A*, 182, 47
- van Straaten S., Ford E. C., van der Klis M., Méndez M., Kaaret P., 2000, *ApJ*, 540, 1049

APPENDIX A: DESCRIPTION OF THE SOURCES

In this appendix we provide detail on the properties of the seven NS qLMXBs in our analyzed sample.

A1 KS 1731–260

The first observation of this source in outburst dates back to 1989 and the detection of X-ray bursts identified it as a NS LMXB (Sunyaev et al. 1989). The source is located in the direction of the Galactic Center and distance estimates suggests that it might be close to it; Munro et al. (2000b) obtained an upper limit of $D < 7$ kpc based on X-ray burst analysis, while Özel et al. (2012) placed the source at ≈ 8 kpc by studying the distribution of stars in its direction. In the same work, the authors analyze multiple X-ray bursts to infer $R < 12$ km and $M < 1.8 M_{\odot}$ as upper limits for the NS parameters.⁶ A NS spin frequency of 524 Hz has been determined from X-ray burst oscillations (1.9 ms; Smith et al. 1997), but the binary orbital period is not known. KS 1731–260 has exhibited only one, ~ 12.5 -year long, historic outburst and has been in quiescence for nearly two decades now. Quiescent X-ray studies revealed a thermally-dominated spectrum and a NS surface temperature that gradually cooled over time (Wijnands et al. 2001b, 2002; Cackett et al. 2006, 2010b; Merritt et al. 2016).

A2 XTE J1701–462

This transient NS LMXB was discovered when it exhibited a luminous outburst in 2006–2007 (Homan et al. 2007). Analysis of its X-ray bursts gave a measurement of the source distance of 8.8 ± 1.3 kpc (Lin et al. 2009). The spin period of the NS or orbital period of the binary are not known, although a large disk and therefore a large orbital period are expected due to its bright outburst. After the end of its outburst, XTE J1701–462 was studied in quiescence which revealed thermal emission from the NS surface, but also a strong and variable hard emission tail, as well as occasional flares that suggest residual accretion occurring in quiescence (Fridriksson et al. 2010, 2011b). No other accretion outbursts have been detected from this source.

A3 MXB 1659–298

Discovered in 1976, MXB 1659–29 was immediately identified as an LMXB harboring a NS due to the detection of X-ray bursts (Lewin et al. 1976). The source shows eclipses every ≈ 7.1 hr, representing the orbital period, which points to a high inclination and proves that it is not an ultra-compact binary (Cominsky & Wood 1984, 1989). The distance of the source is not firmly established: Oosterbroek et al. (2001) studied the X-ray bursts and estimated $D = 11 - 13$ kpc, while Galloway et al. (2008a) point out two different ranges (9 ± 2 and 12 ± 3 kpc) depending on the H content of the material burning during the X-ray burst. Deriving an accurate distance for this source is somewhat hampered by its high inclination, which introduces systematic uncertainties (Galloway et al. 2008b). Rapid variability during the X-ray burst have revealed that the NS spins at 567 Hz (1.67 ms; Wijnands et al. 2001a). Since its discovery outburst in the 1970s, MXB 1659–29 spent most of its time in quiescence, switching on only twice again, in 2001 and in 2015. The source has been observed multiple times in quiescence, revealing a thermally-dominated X-ray spectrum and a gradually decreasing NS temperature (Wijnands et al. 2003, 2004; Cackett et al. 2006, 2013b).

⁶ We note that the “touchdown” method applied for KS 1731–260 (as well as other sources; see Özel & Freire 2016, for a review) has been criticized in a number of works (see e.g. Heinke 2013; Miller & Lamb 2016, for summaries of this discussion). This is mainly because the X-ray bursts used in this approach occur at high accretion rates and therefore the X-ray burst emission may be contaminated by the accretion emission (see Degenaar et al. 2018, for a review), which can introduce biases (e.g. Poutanen et al. 2014; Kajava et al. 2014).

A4 EXO 0748–676

Discovered in 1985 (Parmar et al. 1985), this NS LMXB remained in outburst until 2008. From analyzing its X-ray bursts, a NS spin frequency of 552 Hz (Galloway et al. 2010) and a distance of $D = 7.1 \pm 1.2$ kpc have been inferred (Galloway et al. 2008a). Studying the X-ray eclipses displayed by the source, a high inclination of $i \approx 75^{\circ} - 83^{\circ}$ and an orbital period of 3.82 hr have been inferred (Parmar et al. 1985; Wolff et al. 2009).

After EXO 0748–676 returned to quiescence, it was monitored in X-rays with *Chandra* and *XMM-Newton* (Degenaar et al. 2009, 2011, 2014; Díaz Trigo et al. 2011), primarily to study the thermal evolution of the NS. Its mass and radius have been constrained by Cheng et al. (2017) with the quiescent method applied to *XMM-Newton* data. Interestingly, the authors find different results whether the spectrum was fitted over a range of 0.3–10 keV or 0.5–10 keV. In particular, they find in the former case $M = 2.00^{+0.07}_{-0.24} M_{\odot}$ and $R = 11.3^{+1.3}_{-1.0}$ km, while for the second energy range they obtain $M = 1.50^{+0.4}_{-1.0} M_{\odot}$ and $R = 12.2^{+0.8}_{-3.6}$ km (at 90% confidence level).

Apart from X-ray studies, optical spectroscopic studies of the quiescent counterpart of EXO 0748–676 have put some weak constraints on the NS mass, limiting it to $1.27 \lesssim M \lesssim 2.4 M_{\odot}$ (Bassa et al. 2009; Muñoz-Darias et al. 2009).

A5 Cen X-4

This is the most proximate of the NSs in our sample, with a distance $D = 1.2 \pm 0.3$ kpc determined from the quiescent optical companion (Chevalier et al. 1989). This source was observed for the first time in 1969 during a bright (≈ 20 Crab at peak), two-months lasting outburst (Conner et al. 1969). The system went in outburst a second time ten years later, in 1979 (e.g. Kaluziński et al. 1980), but it has been quiescent ever since. There is no information on the spin period of the NS, but the orbital period has been measured to be 15.1 hr (Chevalier et al. 1989), i.e. the system is not an ultra-compact binary. The main-sequence nature of the companion is confirmed by studies of the optical counterpart (Torres et al. 2002; D’Avanzo et al. 2005). Dynamical mass measurements have been attempted but did not put meaningful constraints on the mass of the NS in Cen X-4 (e.g. McClintock & Remillard 1990; Shahbaz et al. 1993; Torres et al. 2002).

The quiescent X-ray emission of Cen X-4 has been studied extensively with different instruments (e.g. van Paradijs et al. 1987; Asai et al. 1996; Campana et al. 1997, 2000; Cackett et al. 2010a, 2013a; Bernardini et al. 2013; Chakrabarty et al. 2014; D’Angelo et al. 2015). The X-ray spectra always clearly manifest a power-law emission component and like Aql X-1, also Cen X-4 displays clear X-ray variability in quiescence over timescales of years, days and hundreds of seconds. There is strong evidence that residual accretion occurs in quiescence (Cackett et al. 2010a, 2013a; Bernardini et al. 2013; Chakrabarty et al. 2014; D’Angelo et al. 2015). This makes it an interesting comparison with the other NSs in our sample. Cackett et al. (2010a) analyzed several quiescent spectra of Cen X-4 and found that the best-fit radius for the NS is comprised in a 68% confidence range of 7–12.5 km for an assumed mass of $1.5 M_{\odot}$ (using data from *Chandra*, *Suzaku* and *XMM-Newton*).

A6 Aql X-1

This transient NS LMXB was one of the first X-ray sources to be discovered (e.g. Friedman et al. 1967) and has been observed in outburst numerous times since. It displays an accretion outburst about once every year (e.g. Kaluziński et al. 1977; Kitamoto et al. 1993; Campana et al. 2013) and is a known X-ray burster (e.g. Koyama et al. 1981). The X-ray bursts have been used to estimate a distance towards the source of 3.5–4.5 kpc (depending on the composition of the ignition layer; Galloway et al. 2008a), whereas the optical counterpart allows for a distance of 4–8 kpc (Rutledge et al. 2001b; Mata Sánchez et al. 2017). Coherent X-ray pulsations at a frequency of 550 Hz (1.8 ms) revealed the spin period of the NS (Casella et al. 2008). These pulsations were detected only during a single ~ 150 -s long data segment (out of ~ 1 Ms of *RXTE* data), however, and the source is not expected

to be highly magnetised (Di Salvo & Burderi 2003). The companion star has been identified as a late type star of spectral class K7 to M0, orbiting around the compact primary in ≈ 19 hr (Callanan et al. 1999).

Aql X-1 has been extensively studied in quiescence using several different X-ray instruments (e.g. van Paradijs et al. 1987; Verbunt et al. 1994; Rutledge et al. 2002a; Campana & Stella 2003; Cackett et al. 2011; Coti Zelati et al. 2014; Waterhouse et al. 2016; Ootes et al. 2018). It displays a clear thermal emission component, but its quiescent spectra often contain a power-law component too, with a contribution to the overall emission that is highly variable over relatively short timescales (e.g. Rutledge et al. 2002a; Campana & Stella 2003; Cackett et al. 2011; Coti Zelati et al. 2014). Aql X-1 is of particular interest in the context of the present work, because multiple approaches can in principle be used to measure the mass and radius of its NS: Apart from X-ray bursts and quiescent thermal emission, Aql X-1 also exhibits both mHz and kHz QPOs (e.g. Zhang et al. 1998; Revnitsev et al. 2001). Furthermore, its quiescent counterpart is in principle bright enough to obtain dynamical mass measurements (Mata Sánchez et al. 2017).

In a recent work by Li et al. (2017), the methods of obtaining constraints on the mass and radius from quiescent spectra and X-ray bursts (detected with *RXTE*) were simultaneously applied and the results of both techniques compared (assuming different values for the distance). The analysis ellipsoidal regions in a $M - R$ diagram enclosing different ranges as the distance choice changes. For instance, for a distance of 4 (5.5) kpc, the obtained mass and radius regions obtained from the X-ray burst analysis roughly correspond to $M \approx 0.5 - 1.5 M_{\odot}$ and $R \approx 9 - 14$ km ($\approx 1.5 - 2.5 M_{\odot}$ and $R > 12$ km). Using quiescent data from *Chandra* and *XMM-Newton*, on the other hand, the shape of resulting confidence region in $M - R$ space appears more skewed and asymmetrical, and a much less strong dependency on the distance is apparent: for 4 (5.5) kpc, the obtained mass and radius are $M \approx 0.5 - 1.5 M_{\odot}$ and $R \approx 8 - 10$ km ($M \approx 0.5 - 1.8 M_{\odot}$ and $R \approx 8 - 12$ km).⁷ There is only limited overlap in the confidence regions isolated by the two different methods. Li et al. (2017) propose that this could possibly be due to incorrectly assuming a NS atmosphere model for the thermal emission, the lack of spin correction in the quiescent method or to an unconsidered asymmetric expansion of the photosphere during the X-ray bursts.

A7 4U 1608–52

This transient NS LMXB was discovered in the 1970s (Tananabaum et al. 1976) and goes into outburst roughly once every $\sim 1 - 2$ years (e.g. Lochner & Roussel-Dupre 1994; Šimon 2004), during which it exhibits X-ray bursts (e.g. Murakami et al. 1980; Gottwald et al. 1987; Fujimoto & Gottwald 1989; Galloway et al. 2008a). The X-ray bursts have been used to estimate distance of 4U 1608–52, and have been argued to be between 3.4 and 4.2 kpc based on their observed spectral evolution (Ebisuzaki 1987), and between 2.9 and 4.5 kpc based on the peak fluxes of the brightest X-ray bursts (Galloway et al. 2008a). With a completely different method based on the study of the interstellar extinction between the source and the observer, Güver et al. (2010) determined a wider range for the allowed distances of 3.9–7.8 kpc. A study of rapid variability detected during the X-ray bursts (so-called burst oscillations; e.g. Strohmayer et al. 1996) revealed that the NS spins at a high frequency (ν_{spin}) of 620 Hz (Muno et al. 2001; Galloway et al. 2008a). The secondary star is likely to be an H-rich donor star, such as an F- or G-type star, as inferred from the spectrum of the optical counterpart, QX Nor (Wachter et al. 2002). Furthermore the orbital period, never measured but supposedly close to 12 hr from the period of a super-hump, renders it unlikely that the secondary star is a degenerate He-rich star, as in ultra-compact LMXBs (and therefore the NS atmosphere is likely composed of H).

What makes this NS particularly interesting is that it is possible, in theory, to apply several different techniques to estimate its radius. Firstly, from analyzing its X-ray bursts, Poutanen et al. (2014) found $R = 15 -$

21 km for $M = 1.5 M_{\odot}$ and more generally put a lower limit on the NS radius of $R > 12$ km for $M = 1.0 - 2.4 M_{\odot}$.⁸ Secondly, Degenaar et al. (2015) modeled the Fe-K line in the reflection spectrum and obtained an upper limit of $R < 21$ km for the radius of the NS (assuming $M = 1.5 M_{\odot}$). Furthermore, 4U 1608–52 displays both kHz and mHz quasi-periodic oscillations, QPOs (e.g. Berger et al. 1996; Méndez et al. 1998; Jonker et al. 2000; Revnitsev et al. 2001); such signals have been used to place some (weak) constraints on NS radii too (e.g. Miller et al. 1998; Stiele et al. 2016), although not for this particular source.

APPENDIX B: SPECTRAL FITTING RESULTS

In this appendix we provide tables with the results of various X-ray spectral fits for Aql X-1 and EXO 0748–676, i.e. the two sources with the highest quality spectra and the only two for which some constraints on the NS parameters could be obtained. Since the temperature is a parameter left free to vary among the simple spectra in the samples, we report here the average value for the spectra, $\langle \log T_{\text{eff}} \rangle$.

⁷ Li et al. (2017) used a composite model of NSATMOS and an additional power-law component to model the quiescent X-ray spectra.

⁸ We note that Güver et al. (2010) obtained $R = 9.3 \pm 0.1$ km and $M = 1.74 \pm 0.14 M_{\odot}$ for 4U 1608–52 by studying a different sample of bursts. However, Poutanen et al. (2014) argued that this result was likely biased by the artificial cuts in the distance and color correction factor that were made in the analysis.

M (M_{\odot})	0.3-10 keV				0.5-10 keV			
	R (km)	N_{H} (10^{21} cm^{-2})	$\langle \log T_{\text{eff}} \rangle$	χ^2_{ν} (d.o.f.)	R km	N_{H} (10^{21} cm^{-2})	$\langle \log T_{\text{eff}} \rangle$	χ^2_{ν} (d.o.f.)
1.1	11.3±0.6	0.48±0.07	6.24±0.01	1.14(654)	9.8 ^{+0.6} _{-0.6}	0.21±0.09	6.26±0.01	1.07(616)
1.2	11.2 ^{+0.6} _{-0.5}	0.48 ^{+0.08} _{-0.06}	6.24±0.01	1.14(654)	9.6 ^{+0.7} _{-0.5}	0.21 ^{+0.10} _{-0.08}	6.27±0.01	1.07(616)
1.3	11.0 ^{+0.6} _{-0.5}	0.49 ^{+0.08} _{-0.07}	6.25±0.01	1.14(654)	9.2 ^{+0.7} _{-0.5}	0.20 ^{+0.10} _{-0.08}	6.29 ^{+0.01} _{-0.02}	1.07(616)
1.4	10.7 ^{+0.7} _{-0.5}	0.50 ^{+0.08} _{-0.07}	6.26±0.01	1.14(654)	8.9 ^{+0.7} _{-0.5}	0.22 ^{+0.09} _{-0.07}	6.31 ^{+0.01} _{-0.02}	1.07(616)
1.5	10.5 ^{+0.8} _{-0.5}	0.50 ^{+0.07} _{-0.06}	6.28±0.01	1.14(654)	8.2 ^{+0.7} _{-0.5}	0.22 ^{+0.09} _{-0.06}	6.34±0.02	1.07(616)
1.6	10.0 ^{+0.8} _{-0.5}	0.51 ^{+0.08} _{-0.06}	6.29±0.01	1.14(654)	8.2 ^{+0.7} _{-0.5}	0.29 ^{+0.08} _{-0.06}	6.35 ^{+0.02} _{-0.03}	1.07(616)
1.7	9.6 ^{+0.9} _{-0.8}	0.53 ^{+0.07} _{-0.05}	6.31±0.01	1.14(654)	8.5 ^{+0.7} _{-0.5}	0.38 ^{+0.07} _{-0.06}	6.35 ^{+0.02} _{-0.03}	1.08(616)
1.8	9.3 ^{+0.9} _{-0.8}	0.56 ^{+0.07} _{-0.05}	6.34±0.02	1.14(654)	8.9 ^{+0.8} _{-0.5}	0.47 ^{+0.07} _{-0.05}	6.35 ^{+0.02} _{-0.03}	1.10(616)
1.9	9.5 ^{+0.8} _{-0.5}	0.62 ^{+0.06} _{-0.04}	6.33±0.03	1.15(654)	9.4 ^{+0.9} _{-0.5}	0.56 ^{+0.07} _{-0.05}	6.34 ^{+0.02} _{-0.03}	1.12(616)
2.0	9.9 ^{+0.9} _{-0.5}	0.69 ^{+0.06} _{-0.05}	6.33±0.02	1.17(654)	9.9 ^{+0.8} _{-0.6}	0.65 ^{+0.07} _{-0.06}	6.33 ^{+0.02} _{-0.03}	1.15(616)

Table B1. EXO 0748–676. Best-fit radii for different values of the mass, kept frozen during the fits, and best-fit parameters. The values for the distance and normalization of the NSATMOS model were frozen to 7.1 kpc and 1, respectively.

M (M_{\odot})	Mass Variable					Distance Variable					
	R (km)	N_{H} (10^{21} cm^{-2})	Γ	$\langle \log T_{\text{eff}} \rangle$	χ^2_{ν} (d.o.f.)	D (kpc)	R km	N_{H} (10^{21} cm^{-2})	Γ	$\langle \log T_{\text{eff}} \rangle$	χ^2_{ν} (d.o.f.)
1.1	12.9 ^{+1.9} _{-1.4}	4.1 ^{+0.3} _{-0.2}	1.2 ^{+0.5} _{-0.4}	6.19 ^{+0.02} _{-0.03}	0.87(541)	4.0	9.4 ^{+0.9} _{-1.4}	4.2±0.3	1.1±0.4	6.23 ^{+0.03} _{-0.04}	0.81(342)
1.2	12.5 ^{+1.8} _{-1.4}	4.1 ^{+0.3} _{-0.2}	1.1±0.4	6.19 ^{+0.02} _{-0.03}	0.87(541)	4.5	11.5 ^{+1.7} _{-1.2}	4.1 ^{+0.4} _{-0.3}	1.1±0.4	6.20 ^{+0.02} _{-0.03}	0.87(541)
1.3	12.0 ^{+2.0} _{-1.4}	4.1 ^{+0.3} _{-0.2}	1.1 ^{+0.5} _{-0.3}	6.20 ^{+0.02} _{-0.03}	0.87(541)	5.0	12.2 ^{+1.9} _{-1.3}	4.1 ^{+0.3} _{-0.2}	1.1 ^{+0.5} _{-0.3}	6.21 ^{+0.02} _{-0.03}	0.87(541)
1.4	12.2 ^{+1.9} _{-1.3}	4.1 ^{+0.3} _{-0.2}	1.1 ^{+0.5} _{-0.3}	6.21 ^{+0.02} _{-0.03}	0.87(541)	5.5	13.3 ^{+1.7} _{-1.5}	4.1 ^{+0.4} _{-0.1}	1.1 ^{+0.5} _{-0.3}	6.21 ^{+0.01} _{-0.04}	0.87(541)
1.5	11.8 ^{+1.2} _{-0.6}	4.1 ^{+0.3} _{-0.2}	1.1 ^{+0.5} _{-0.3}	6.19 ^{+0.02} _{-0.03}	0.87(541)	6.0	14.4 ^{+2.6} _{-1.8}	4.1 ^{+0.4} _{-0.2}	1.1 ^{+0.5} _{-0.3}	6.20 ^{+0.02} _{-0.03}	0.87(541)
1.6	12.0 ^{+2.0} _{-1.4}	4.2 ^{+0.3} _{-0.2}	1.1 ^{+0.4} _{-0.4}	6.21 ^{+0.02} _{-0.04}	0.87(541)	6.5	15.4 ^{+2.0} _{-1.9}	4.1 ^{+0.4} _{-0.2}	1.2 ^{+0.4} _{-0.3}	6.20 ^{+0.02} _{-0.03}	0.87(541)
1.7	11.0 ^{+2.0} _{-1.1}	4.1 ^{+0.3} _{-0.2}	1.1±0.4	6.21 ^{+0.03} _{-0.04}	0.87(541)	7.0	16.4 ^{+2.0} _{-1.8}	4.1 ^{+0.4} _{-0.2}	1.1 ^{+0.5} _{-0.3}	6.20 ^{+0.02} _{-0.03}	0.87(541)
1.8	12.0 ^{+2.0} _{-1.2}	4.1 ^{+0.3} _{-0.2}	1.1 ^{+0.5} _{-0.3}	6.24 ^{+0.03} _{-0.04}	0.87(541)	7.5	17.9 ^{+2.5} _{-1.7}	4.1 ^{+0.4} _{-0.2}	1.1 ^{+0.5} _{-0.3}	6.20 ^{+0.02} _{-0.03}	0.87(541)
1.9	12.0 ^{+2.0} _{-1.1}	4.2±0.2	1.2 ^{+0.4} _{-0.3}	6.25 ^{+0.03} _{-0.03}	0.87(541)	8.0	18.0±2.0	4.1 ^{+0.4} _{-0.2}	1.1 ^{+0.5} _{-0.3}	6.20 ^{+0.02} _{-0.03}	0.87(541)
2.0	12.0 ^{+2.0} _{-1.2}	4.3±0.3	1.2 ^{+0.4} _{-0.3}	6.26 ^{+0.03} _{-0.06}	0.87(541)						

Table B2. Aql X-1 full sample. Left: Best-fit radii for different values of the mass, kept frozen during the fits, and best-fit parameters. The value for the distance was frozen at 5 kpc. Right: Best-fit radii for different values of the distance, kept frozen during the fits, and best-fit parameters. The value for the mass has been kept frozen to 1.4 M_{\odot} . The normalization for the NSATMOS model and the energy range for PEGPWRLW were frozen in both series of fits to values of 1 and 0.5–10 keV, respectively. These results refer to the final, all-inclusive sample of the 14 available *Chandra* observations.

M (M_{\odot})	Mass Variable				Distance Variable				
	R (km)	N_{H} (10^{21} cm^{-2})	$\langle \log T_{\text{eff}} \rangle$	χ^2_{ν} (d.o.f.)	D (kpc)	R km	N_{H} (10^{21} cm^{-2})	$\langle \log T_{\text{eff}} \rangle$	χ^2_{ν} (d.o.f.)
1.1	5.0 ^{+1.3} _{-5.0}	3.17±0.16	6.44 ^{+0.01} _{-0.08}	1.53(203)	4.0	7.00 ^{+1.00} _{-0.60}	4.20±0.20	6.34 ^{+0.05} _{-0.06}	1.68(203)
1.2	5.2 ^{+0.7} _{-0.1}	3.40±0.15	6.44 ^{+0.01} _{-0.08}	1.55(203)	4.5	7.00 ^{+0.90} _{-0.70}	3.90±0.20	6.36 ^{+0.05} _{-0.09}	1.64(203)
1.3	5.8 ^{+1.6} _{-1.0}	3.60±0.20	6.42 ^{+0.03} _{-0.09}	1.57(203)	5.0	6.4 ^{+1.0} _{-0.5}	3.73±0.19	6.43 ^{+0.05} _{-0.14}	1.60(203)
1.4	6.4 ^{+1.0} _{-0.5}	3.73 ^{+0.19} _{-0.14}	6.43 ^{+0.03} _{-0.08}	1.60(203)	5.5	6.20 ^{+1.40} _{-0.50}	3.30±0.20	6.45 ^{+0.08} _{-0.09}	1.56(203)
1.5	6.7 ^{+1.2} _{-0.6}	3.90 ^{+0.19} _{-0.16}	6.41 ^{+0.05} _{-0.10}	1.63(203)	6.0	6.10 ^{+0.67} _{-0.05}	3.40 ^{+0.17} _{-0.30}	6.45 ^{+0.03} _{-0.06}	1.54(203)
1.6	8.1 ^{+1.2} _{-1.0}	4.10 ^{+0.20} _{-0.19}	6.36 ^{+0.05} _{-0.10}	1.66(203)	6.5	6.02 ^{+0.45} _{-0.01}	3.20 ^{+0.20} _{-0.30}	6.46 ^{+0.02} _{-0.07}	1.53(203)
1.7	8.3 ^{+1.4} _{-0.9}	4.20 ^{+0.20} _{-0.18}	6.35 ^{+0.05} _{-0.08}	1.69(203)	7.0	6.50 ^{+0.30} _{-0.20}	3.10 ^{+0.20} _{-0.30}	6.47 ^{+0.01} _{-0.10}	1.52(203)
1.8	8.8 ^{+1.3} _{-1.1}	4.30±0.20	6.34 ^{+0.05} _{-0.07}	1.72(203)	7.5	6.30 ^{+0.60} _{-0.05}	2.90 ^{+0.20} _{-0.30}	6.47 ^{+0.01} _{-0.10}	1.51(203)
1.9	9.3 ^{+1.3} _{-1.1}	4.40±0.20	6.33 ^{+0.03} _{-0.05}	1.75(203)	8.0	6.50 ^{+0.70} _{-0.05}	2.80 ^{+0.20} _{-0.30}	6.47 ^{+0.01} _{-0.10}	1.51(203)
2.0	9.8 ^{+1.6} _{-1.4}	4.60±0.20	6.33 ^{+0.04} _{-0.05}	1.78(203)					

Table B3. Aql X-1 "No Power-Law" sample. Left: Best-fit radii for different values of the mass, kept frozen during the fits, and best-fit parameters. The value for the distance was frozen at 5 kpc. Right: Best-fit radii for different values of the distance, kept frozen during the fits, and best-fit parameters. The value for the mass has been kept frozen to 1.4 M_{\odot} . The normalization for the NSATMOS model and the energy range for PEGPWRLW were frozen in both series of fits to values of 1 and 0.5–10 keV, respectively.

Mass Variable						Distance Variable					
M (M_{\odot})	R (km)	N_{H} (10^{21} cm^{-2})	Γ	$\langle \log T_{\text{eff}} \rangle$	χ^2_{ν} (d.o.f.)	D (kpc)	R km	N_{H} (10^{21} cm^{-2})	Γ	$\langle \log T_{\text{eff}} \rangle$	χ^2_{ν} (d.o.f.)
1.1	$12.5^{+2.2}_{-1.3}$	$4.1^{+0.4}_{-0.2}$	1.2 ± 0.05	$6.19^{+0.04}_{-0.02}$	0.81(342)	4.0	$9.3^{+1.7}_{-1.4}$	4.1 ± 0.2	$1.2^{+0.5}_{-0.4}$	$6.24^{+0.04}_{-0.05}$	0.81(335)
1.2	$13.2^{+2.7}_{-1.7}$	$4.1^{+0.4}_{-0.3}$	$1.3^{+0.5}_{-0.4}$	$6.19^{+0.03}_{-0.04}$	0.81(342)	4.5	$7.0^{+5.3}_{-0.5}$	$4.1^{+0.8}_{-0.2}$	$1.2^{+0.4}_{-0.9}$	6.29 ± 0.03	0.81(335)
1.3	$12.3^{+2.4}_{-1.2}$	$4.1^{+0.4}_{-0.3}$	1.2 ± 0.5	$6.21^{+0.02}_{-0.06}$	0.81(342)	5.0	$12.8^{+3.4}_{-1.1}$	$4.2^{+0.5}_{-0.2}$	$1.2^{+0.6}_{-0.3}$	$6.21^{+0.02}_{-0.06}$	0.81(335)
1.4	$12.8^{+3.4}_{-1.1}$	$4.2^{+0.5}_{-0.2}$	$1.2^{+0.6}_{-0.3}$	$6.21^{+0.02}_{-0.06}$	0.81(335)	5.5	$13.2^{+2.2}_{-1.7}$	4.1 ± 0.3	$1.2^{+0.5}_{-0.4}$	$6.20^{+0.03}_{-0.04}$	0.81(335)
1.5	$12.0^{+2.6}_{-1.1}$	$4.1^{+0.4}_{-0.2}$	1.2 ± 0.5	$6.22^{+0.04}_{-0.05}$	0.81(342)	6.0	$14.3^{+2.4}_{-2.0}$	4.1 ± 0.3	1.2 ± 0.5	$6.20^{+0.03}_{-0.04}$	0.81(335)
1.6	$11.8^{+2.3}_{-1.6}$	$4.1^{+0.4}_{-0.2}$	$1.2^{+0.5}_{-0.4}$	$6.23^{+0.04}_{-0.05}$	0.81(342)	6.5	$15.0^{+3.0}_{-2.0}$	4.1 ± 0.3	$1.2^{+0.3}_{-0.4}$	$6.20^{+0.03}_{-0.04}$	0.81(335)
1.7	11.0 ± 2.0	4.1 ± 0.3	1.2 ± 0.4	$6.25^{+0.05}_{-0.08}$	0.81(342)	7.0	$16.0^{+3.0}_{-2.0}$	$4.1^{+0.4}_{-0.3}$	$1.2^{+0.5}_{-0.4}$	$6.20^{+0.03}_{-0.04}$	0.81(335)
1.8	$10.3^{+2.2}_{-1.8}$	$4.1^{+0.3}_{-0.2}$	$1.1^{+0.5}_{-0.3}$	$6.28^{+0.06}_{-0.08}$	0.81(342)	7.5	$18.0^{+3.0}_{-2.0}$	$4.1^{+0.4}_{-0.3}$	$1.2^{+0.6}_{-0.4}$	$6.19^{+0.03}_{-0.04}$	0.81(335)
1.9	$9.8^{+2.5}_{-1.9}$	4.1 ± 0.2	$1.2^{+0.3}_{-0.4}$	$6.30^{+0.06}_{-0.08}$	0.82(342)	8.0	$18.0^{+3.0}_{-2.0}$	$4.0^{+0.4}_{-0.3}$	$1.2^{+0.4}_{-0.4}$	$6.20^{+0.03}_{-0.04}$	0.81(335)
2.0	$10.4^{+2.7}_{-1.8}$	4.2 ± 0.2	1.3 ± 0.4	$6.29^{+0.06}_{-0.08}$	0.81(342)						

Table B4. Aql X-1 "Power-Law" sample. Left: Best-fit radii for different values of the mass, kept frozen during the fits, and best-fit parameters. The value for the distance was frozen at 5 kpc. Right: Best-fit radii for different values of the distance, kept frozen during the fits, and best-fit parameters. The value for the mass has been kept frozen to $1.4 M_{\odot}$. The normalization for the NSATMOS model and the energy range for PEGPWRLW were frozen in both series of fits to values of 1 and 0.5–10 keV, respectively.

Mass Variable					Distance Variable				
M (M_{\odot})	R (km)	N_{H} (10^{21} cm^{-2})	$\langle \log T_{\text{eff}} \rangle$	χ^2_{ν} (d.o.f.)	D (kpc)	R km	N_{H} (10^{21} cm^{-2})	$\langle \log T_{\text{eff}} \rangle$	χ^2_{ν} (d.o.f.)
1.1	$13.2^{+2.2}_{-1.5}$	$4.2^{+0.4}_{-0.3}$	$6.17^{+0.02}_{-0.03}$	0.98(197)	4.0	$10.6^{+1.9}_{-1.1}$	$4.2^{+0.3}_{-0.2}$	$6.20^{+0.03}_{-0.04}$	0.98(197)
1.2	$13.2^{+2.2}_{-1.6}$	$4.2^{+0.4}_{-0.3}$	$6.18^{+0.02}_{-0.03}$	0.98(197)	4.5	$12.0^{+2.0}_{-1.3}$	$4.2^{+0.4}_{-0.3}$	$6.19^{+0.03}_{-0.04}$	0.98(197)
1.3	$13.2^{+2.2}_{-1.5}$	$4.2^{+0.4}_{-0.3}$	$6.18^{+0.02}_{-0.03}$	0.98(197)	5.0	$13.6^{+2.9}_{-1.3}$	$4.2^{+0.4}_{-0.3}$	$6.18^{+0.02}_{-0.03}$	0.98(197)
1.4	$13.6^{+2.9}_{-1.3}$	$4.2^{+0.4}_{-0.3}$	$6.18^{+0.02}_{-0.03}$	0.98(197)	5.5	$14.2^{+2.5}_{-1.7}$	$4.2^{+0.4}_{-0.3}$	$6.19^{+0.02}_{-0.03}$	0.98(197)
1.5	$13.3^{+2.4}_{-1.4}$	$4.2^{+0.4}_{-0.3}$	$6.19^{+0.04}_{-0.02}$	0.98(197)	6.0	$15.3^{+2.5}_{-1.7}$	$4.2^{+0.4}_{-0.3}$	$6.19^{+0.03}_{-0.03}$	0.98(197)
1.6	$12.7^{+2.0}_{-1.4}$	$4.2^{+0.4}_{-0.3}$	$6.20^{+0.04}_{-0.03}$	0.98(197)	6.5	$16.0^{+3.0}_{-2.0}$	$4.2^{+0.4}_{-0.3}$	$6.19^{+0.02}_{-0.03}$	0.98(197)
1.7	$13.0^{+2.0}_{-1.4}$	4.2 ± 0.3	$6.21^{+0.03}_{-0.04}$	0.98(197)	7.0	$17.0^{+3.0}_{-2.0}$	4.1 ± 0.4	$6.19^{+0.02}_{-0.03}$	0.98(197)
1.8	$12.0^{+2.2}_{-1.4}$	4.2 ± 0.3	$6.23^{+0.03}_{-0.04}$	0.98(197)	7.5	$18.0^{+3.0}_{-2.0}$	$4.1^{+0.3}_{-0.2}$	$6.19^{+0.02}_{-0.03}$	0.98(197)
1.9	$12.7^{+2.1}_{-1.4}$	4.3 ± 0.3	$6.22^{+0.03}_{-0.04}$	0.98(197)	8.0	$19.0^{+3.0}_{-2.0}$	$4.1^{+0.4}_{-0.3}$	$6.19^{+0.02}_{-0.03}$	0.98(197)
2.0	$12.5^{+2.2}_{-1.4}$	$4.4^{+0.3}_{-0.2}$	$6.23^{+0.03}_{-0.04}$	0.98(197)					

Table B5. Aql X-1 sample originally indicated as "No Power-Law" but now with a $\Gamma = 1.2$ power-law component added. Left: Best-fit radii for different values of the mass, kept frozen during the fits, and best-fit parameters. The value for the distance was frozen at 5 kpc. Right: Best-fit radii for different values of the distance, kept frozen during the fits, and best-fit parameters. The value for the mass has been kept frozen to $1.4 M_{\odot}$. The normalization for the NSATMOS model and the energy range for PEGPWRLW were frozen in both series of fits to values of 1 and 0.5–10 keV, respectively.

D (kpc)	R (km)	N_{H} (10^{21} cm^{-2})	$\langle \log T_{\text{eff}} \rangle$	χ^2_{ν} (d.o.f.)
6.1	$8.9^{+0.7}_{-0.5}$	$0.52^{+0.08}_{-0.06}$	$6.28^{+0.01}_{-0.02}$	1.14(654)
6.6	$9.6^{+0.8}_{-0.5}$	$0.49^{+0.09}_{-0.06}$	$6.27^{+0.01}_{-0.02}$	1.14(654)
7.1	$10.7^{+0.7}_{-0.5}$	$0.50^{+0.08}_{-0.07}$	6.26 ± 0.01	1.14(654)
7.6	$11.5^{+0.8}_{-0.6}$	$0.48^{+0.08}_{-0.06}$	6.25 ± 0.01	1.14(654)
8.1	$12.4^{+0.7}_{-0.6}$	$0.48^{+0.08}_{-0.07}$	6.25 ± 0.01	1.14(654)

Table B6. EXO 0748–676. Best-fit radii for different values of the distance, kept frozen during the fits, and best-fit parameters. The values for the mass and normalization of the NSATMOS model were frozen to $1.4 M_{\odot}$ and 1, respectively.